

1 **Temporal-specific roles of Fragile X mental retardation protein in the development of**
2 **hindbrain auditory circuit**

3
4 Xiaoyu Wang^{*1,2}, Ayelet Kohl^{*3}, Xiaoyan Yu¹, Diego A. R. Zorio¹, Avihu Klar⁴, Dalit Sela-
5 Donenfeld^{#3} and Yuan Wang^{#1}

6
7 * Equal first authors

8 # Equal corresponding authors

9 1. Department of Biomedical Sciences, Program in Neuroscience, Florida State University
10 College of Medicine, Tallahassee, FL 32306, USA

11 2. Division of Histology & Embryology, Key Laboratory for Regenerative Medicine of the Ministry
12 of Education, Medical College, Jinan University, Guangzhou 510632, China

13 3. Koret School of Veterinary Medicine, Robert H. Smith Faculty of Agriculture, Food and
14 Environment, The Hebrew University of Jerusalem, Rehovot 76100, Israel

15 4. Department of Medical Neurobiology IMRIC, Hebrew University Medical School, Jerusalem
16 91120, Israel

17

18 **Running title:** FMRP in young hindbrain axons

19

20 **Corresponding Authors:**

21 Yuan Wang, Ph.D.

22 1115 West Call Street, Florida State University, Tallahassee, FL 32306, USA

23 Phone: (850) 645-4934; Email: yuan.wang@med.fsu.edu

24

25 Dalit Sela-Donenfeld, Ph.D.

26 Koret School of Veterinary Medicine, The Hebrew University of Jerusalem, Rehovot 76100,
27 Israel

28 Phone: (972) 89489533; Email: dalit.seladon@mail.huji.ac.il

29

30 **Keywords:** Crispr-Cas9; auditory circuit; Fragile X syndrome; autism spectrum disorder; RNA-
31 binding proteins; axon development; axon fasciculation; axon targeting

32

33 **Summary Statement**

34 Deficiency of an RNA-binding protein, FMRP, negatively affects how auditory axons travel
35 through the developing brainstem and establish proper synaptic connectivity in a timely manner.

36

37

38 **Abstract**

39 Fragile X mental retardation protein (FMRP) is an RNA-binding protein abundant in the nervous
40 system. Functional loss of FMRP leads to sensory dysfunction and severe intellectual
41 disabilities. In the auditory system, FMRP deficiency alters neuronal function and synaptic
42 connectivity and results in perturbed processing of sound information. Nevertheless, roles of
43 FMRP in embryonic development of the auditory hindbrain have not been identified. Here, we
44 developed high-specificity approaches to genetically track and manipulate throughout
45 development the Atoh1⁺ neuronal cell type, which is highly conserved in vertebrates, in the
46 cochlear nucleus of chicken embryos. [We identified distinct FMRP-containing granules in the
47 growing axons of Atoh1⁺ neurons and post-migrating NM cells.](#) FMRP downregulation via
48 Crispr/Cas9 and shRNA techniques resulted in perturbed axonal pathfinding, delay in midline
49 crossing, excess branching of neurites, and axonal targeting errors during the period of circuit
50 development. Together, these results provide the first *in vivo* identification of FMRP localization
51 and actions in developing axons of auditory neurons, and demonstrate the importance of
52 investigating early embryonic alterations toward understanding the pathogenesis of
53 neurodevelopmental disorders.

54

55 **Introduction**

56 The Fragile X mental retardation protein (FMRP; encoded by *Fmr1* gene) is an RNA-binding
57 protein that regulates many aspects of gene expression and protein function (Bagni and
58 Greenough, 2005; Bassell and Warren, 2008; Davis and Broadie, 2017). Functional loss of
59 FMRP during development leads to Fragile X syndrome (FXS), an intellectual disability. Many
60 FXS symptoms appear early in life, including increasing autism features and emerging sensory
61 hyperarousal, anxiety, and hyperactivity (Hagerman et al., 2017). These clinical observations,
62 along with FMRP expression throughout gestation (Abitbol et al., 1993; Hinds et al., 1993),
63 implicate a role of FMRP in embryonic and early postnatal brains. While FMRP regulation of
64 neurotransmission and synaptic plasticity plays important roles in relatively mature brains (Bagni
65 and Zukin, 2019; Bear et al., 2004; Deng et al., 2013; Ferron et al., 2014), how FMRP regulates
66 brain development during embryonic stages is largely unknown, except its involvement in
67 cortical neurogenesis (Castrén, 2016).

68 Axon growth is a multi-event process of embryonic brain development, including
69 axonogenesis, pathfinding, arborizing, and terminating on appropriate postsynaptic structures
70 (reviewed in Chédotal and Richards, 2010; Comer et al., 2019; Stoeckli, 2018). Multiple lines of
71 evidence support an involvement of FMRP in axonal development. In the *Drosophila* mushroom
72 body, FMRP limits axonal growth and controls axonal pruning (Bodaleo and Gonzalez-Billault,
73 2016; Pan et al., 2004; Tessier and Broadie, 2008). In vertebrates, FMRP knockout results in
74 excessive axonal branches in zebrafish motor neurons (Shamay-Ramot et al., 2015) and
75 abnormal projection patterns in the mouse forebrain (Bureau et al., 2008; Scharkowski et al.,
76 2018). FMRP also associates with RNAs that encode proteins involved in axonogenesis and
77 synaptogenesis, including the microtubule-associated protein MAP1b (Bodaleo and Gonzalez-
78 Billault, 2016), cell adhesion molecule Dscam (Jain and Welshhans, 2016), and the axon
79 guidance cue netrin (Kang et al., 2019). However, the exact *in vivo* functions of FMRP in distinct
80 axonal events are unclear.

81 Here, we investigated the roles of FMRP in axonal development of the auditory
82 brainstem using the chick embryo as a model system. The avian nucleus magnocellularis (NM)
83 and nucleus laminaris (NL) are structurally and functionally similar to the mammalian
84 anteroventral cochlear nucleus (AVCN) and medial superior olive (MSO), respectively.
85 NM/AVCN neurons receive temporally precise excitation from the auditory nerve, and in turn,
86 send bilaterally segregated signals to NL/MSO. Bipolar neurons in NL and MSO are specialized
87 to compute interaural time differences (ITDs), time disparities in the arrival of signals between
88 the two ears, binaural cues critical for sound localization and segregation (Nothwang, 2016;

89 Overholt et al., 1992; Vonderschen and Wagner, 2014). Clinical studies have revealed a tight
90 association between FMRP level and temporal performance and have found impaired temporal
91 processing of visual and auditory information in FXS (Farzin et al., 2011; Hall et al., 2009; Kéri
92 and Benedek, 2011; Kogan et al., 2004; Rais et al., 2018). Cellular studies have further
93 identified structural and physiological abnormalities in AVCN and its target cell groups in FMRP
94 knockout rodents (Brown et al., 2010; El-Hassar et al., 2019; Garcia-Pino et al., 2017; Lu, 2019;
95 McCullagh et al., 2017; Rotschafer et al., 2015; Ruby et al., 2015; Strumbos et al., 2010; Wang
96 et al., 2015a). Finally, the nucleotide and amino acid sequences of chicken FMRP are similar to
97 human FMRP (Price et al., 1996; Wang et al., 2014). Thus, studying FMRP regulation of NM
98 and NL neurons is functionally relevant toward understanding FXS. Additionally, the stereotyped
99 pattern of axonal projection from NM to NL (**Fig. 1A**) provides a suitable model for mechanistic
100 studies of axonal circuitry development (Allen-Sharpley and Cramer, 2012; Cramer et al., 2004;
101 Seidl et al., 2014).

102 To track specific cell types and neural circuits in complex vertebrate brains, we
103 developed several genetic tools to selectively label and manipulate NM precursors and neurons
104 in developing chicken embryos. [We have identified an early-onset FMRP localization in axons of](#)
105 [NM precursors and neurons](#) and discovered that FMRP is required for the orderly and timely
106 development of multiple axon events. These findings provide novel insights into understanding
107 the potential contribution of compromised embryonic brain development to FXS pathogenesis.

108

109 **Results**

110 **Dissecting the axonal circuitry development of NM precursors and neurons**

111 NM neurons project to NL bilaterally (**Fig. 1A**). NL neurons are bipolar, with dendrites extending
112 dorsally and ventrally from the soma to form two segregated dendritic domains. Cell bodies of
113 NL neurons align into a single sheet, resulting in separate dorsal and ventral dendritic neuropil
114 laminae. Individual NM axons bifurcate and project to the dorsal neuropil of the ipsilateral NL
115 and the ventral neuropil of the contralateral NL. This segregated innervation pattern forms the
116 anatomical substrate for ITD computation.

117 To label NM precursors and neurons selectively, we combined genetic markers with
118 spatially controlled plasmid expression (**Fig. 1B**). The progenitor dA1 cells located along the
119 dorsal-most region of the caudal rhombic lip expresses a basic helix-loop-helix transcription
120 factor atonal homolog 1 (Atoh1), which gives rise to excitatory neurons in the auditory brainstem
121 and precerebellar nuclei (Fargo et al., 2006; Fujiyama et al., 2009; Helms et al., 2000; Machold
122 and Fishell, 2005; Maricich et al., 2009). To enhance the specific labeling of the auditory

123 neurons, we introduced a plasmid expressing the Atoh1-enhancer element upstream to Cre
124 recombinase along with a Cre-dependent myristoylated-GFP (mGFP) reporter plasmid into
125 rhombomeres 5-6 (r5-6), which contain NM and NL precursors, via *in ovo* electroporation
126 (Avraham et al., 2009; Cramer et al., 2000; Helms et al., 2000; Kohl et al., 2012; Kohl et al.,
127 2013; Lipovsek and Wingate, 2018; **Fig. S1**). The electroporated Cre-conditional mGFP
128 sequence was integrated into the chick genome by applying the PiggyBac transposition method
129 (Wang et al., 2009), allowing the prolonged expression of the reporter in the auditory neurons
130 (Hadas et al., 2014; Lu et al., 2009). For more restricted NM labeling, we performed the
131 electroporation at E2-2.5, before NL cells are born (Rubel et al., 1976). Following
132 electroporation, mGFP⁺ cell bodies exhibited a restricted distribution in anatomically defined NM
133 on the transfected side when examined at later stages (**Fig. 1C**). Axons of mGFP⁺ cells
134 originated from NM and projected to NL bilaterally, exhibiting the characterized pattern of NM-
135 NL projection (**Fig. 1C, D**). **The transfection rate, as calculated as the percentage of mGFP⁺**
136 **neurons among all neurons in NM, was 15.3% ± 10.3% (mean ± SD; n=8 embryos) ranging**
137 **from 3.4% to 34.4% (Fig. 1E).** No mGFP⁺ cells were detected in the contralateral NM, NL, or
138 surrounding brainstem regions. Thus, our genetic targeting of Atoh1-mGFP cells was
139 predominantly the NM precursors, termed *Atoh1 precursors of NM* henceforth, that establish the
140 NM-NL circuit.

141 Next, we examined the development of the NM circuit stage by stage. We previously
142 demonstrated that Atoh1/dA1 cells across r2-7 give rise to two contralateral axon projections
143 (Kohl et al., 2012; 2015). One projection originated from the caudal hindbrain and elongated in a
144 dorsal funiculus (DF), while the other arose from the more anterior hindbrain and formed a
145 lateral funiculus (LF; **Fig. 2A**). The *Atoh1 precursors of NM* located at r5-6 extended their axons
146 within the DF bundle (**Fig. 2B**). **On transverse sections at E4.5, mGFP⁺ axons had crossed the**
147 **midline and arrived at the location where the NM and NL will form (yellow arrows in Fig. 2C), as**
148 **indicated by a midline crossing rate of 1.060 (n=7 embryos; Fig. 2D-E).** On the ipsilateral side,
149 **mGFP⁺ axons form a well-defined dorsal-to-ventral fascicule (white arrow in Fig. 2C), confirmed**
150 **quantitatively by small axonal bundle width ratio (0.259, n=7 embryos; Fig. 2D, F).** At E7, NL
151 was separating from the NM with rostral-to-caudal progress (**Fig. S2**), consistent with a previous
152 report (Hendricks et al., 2006). mGFP⁺ axons arrived at the emerging NL on the contralateral
153 side (white arrows). In contrast, the ipsilateral projection was not visible, which is consistent with
154 the results of individual axonal reconstructions that showed no ipsilateral projection until E8
155 (Young and Rubel, 1986). At E9 and later, NM and NL were recognizable as individual nuclei.
156 The ipsilateral projection of mGFP⁺ cells to the dorsal neuropil of NL had formed, revealing the

157 characterized bilateral NM-NL projection (Fig.S2). To further confirm this connectivity at the
158 synaptic level, E2 embryos were electroporated with SV2-GFP along with Atoh1 enhancers and
159 the PiggyBac transposase (Fig. 2G), enabling the expression of GFP in presynaptic vesicles
160 (Hadas et al., 2014; Kohl et al., 2012). SV2-GFP was detected in the dorsal NL ipsilaterally and
161 ventral NL contralaterally at E9 (Fig. 2H-I'), confirming the segregated synaptic projection from
162 Atoh1-NM neurons to NL.

163 Closer examination of NM axons within NL revealed a stage-dependent terminal
164 maturation (Fig. 3). At E11-13, the incoming NM axons ended with a typical growth cone
165 morphology with 1-5 filopodia (white arrows). These filopodia gradually disappeared and turned
166 into bouton endings at E15 (yellow arrows). By post-hatch day 6 (P6), NM axons exhibited a
167 mature terminal morphology (Fig. S3, S4). Immunostaining demonstrated a distribution of
168 vesicular glutamate transporters (vGluT2) along the axon course of Atoh1 precursors of NM at
169 E4.5 (Fig. S5). At E15, NM axonal terminals contain a presynaptic SNARE component,
170 SNAP25 (Fig. S6), indicating functional synapses. The time frame of the terminal morphological
171 change was similar between the ipsilateral and contralateral projections of NM neurons, which
172 indicates that the maturation of presynaptic terminals from the two NM inputs to NL neurons is
173 temporally synchronized, although the two inputs differ in their time of arrival at the target area.

174

175 **Axonal localization of FMRP in NM precursors and neurons**

176 FMRP is strongly expressed in hindbrain (Fig. 4A). It is not known whether FMRP is localized in
177 NM axons, and if so, when this localization emerges during development. Here, we addressed
178 this question by immunostaining endogenous FMRP and localizing ectopic FMRP. Embryos
179 were electroporated with Atoh1-mGFP at E2. At E4-5 (n=5 embryos), mGFP⁺ cells consistently
180 showed somatic FMRP immunoreactivity (Fig. 4B-B'', 4C-C''). Contralaterally, mGFP⁺ axons
181 terminated in a cell-free region where FMRP staining is generally low (yellow arrows in Fig. 4B-
182 B''). Closer observation demonstrated distinct FMRP puncta in this region (Fig. 4D'). These
183 puncta were 0.2 to 0.7 μm in diameter, with an average density of 4.3 puncta per 100 μm^2 (28
184 sections from 5 embryos). A subset of FMRP puncta overlapped with mGFP⁺ axon processes
185 (Fig. 4D- E), confirming FMRP localization in distal axons of NM precursors.

186 We next determined whether FMRP is localized in NM axons at late embryonic stages
187 when they have formed synaptic connectivity with NL neurons. During this time window (E9 to
188 E19), the neuropil regions of NL contain a mixture of NM axons, NL dendrites, and astrocyte
189 processes. We developed a transposon-based vector system expressing chick FMRP
190 (chFMRP) fused with mCherry (Fig. 5A) for constitutive expression (Schechter et al., 2012).

191 At E4, mCherry⁺ puncta were identified in the fibrous area where contralateral axons of NM
192 precursors terminate (**Fig. S7**), consistent with the localization of endogenous FMRP puncta
193 shown in Fig. 4. We co-electroporated E2 embryos with chFMRP-mCherry and Atoh1-mGFP
194 (**Fig. 5B**) and harvested brainstem sections between E9 and E19 (n=13 embryos). A substantial
195 number of NM cells expressed chFMRP-mCherry on the transfection side (**Fig. 5C**, left column).
196 In addition, mCherry⁺ NL neurons were seen on the same side in some cases. To avoid this
197 confounding factor, further analyses were performed in the contralateral NL in which mCherry
198 labeling was exclusively derived from transfected NM axons. Across all cases, mCherry⁺ puncta
199 were identified in the fiber region between NL and the ventral brainstem, which contains
200 incoming NM axons, as well as within the ventral neuropil domain of NL (**Fig. 5C**, right column).
201 This localization pattern indicates that the introduced chicken FMRP is localized in the distal
202 portions of NM axons. This is further confirmed by the presence of mCherry⁺ puncta in Atoh1-
203 mGFP expressing axons (**Fig. 5D**). Next, we replaced chFMRP-mCherry with human FMRP
204 (hFMRP)-EGFP in the plasmid (**Fig. 5A**) and identified a similar pattern of FMRP distribution
205 (**Fig. 5E**). This result implicates that the sequence of FMRP underlying its axon localization in
206 NM axons is conserved between birds and humans.

207

208 **FMRP deficiency affects axonal growth pattern of NM precursors**

209 In vitro studies implicate FMRP regulation in neurite outgrowth (Doers et al., 2014), axon
210 elongation (Wang et al., 2015b), and branching (Zimmer et al., 2017). Together with our finding
211 that *Atoh1* precursors of NM contain FMRP in distal axons (Fig. 4), these studies raise the
212 possibility that FMRP regulates axonal growth and pathfinding of NM precursors *in vivo*. We
213 examined this possibility by determining the effects of downregulating FMRP on axon
214 development of *Atoh1* precursors of NM.

215 Crispr-mediated FMRP knockout. We first downregulated FMRP in Atoh1⁺ neurons
216 using the Crispr (clustered regularly interspaced short palindromic repeats)/Cas9 system (Cong
217 et al., 2013; Hille and Charpentier, 2016). Two guide RNAs (gRNA₃ and gRNA₄) were designed
218 to target exon 8 of FMRP coding sequence to cause a deletion of ~260 bp (**Fig. 6A; Table 1**).
219 To verify this deletion, gRNA₃₊₄ plasmids, which contain Cas9 and GFP on the same pCAG-
220 construct, were co-electroporated into the dorsal-most region of E2.5 embryos. Control embryos
221 were electroporated with a control-gRNA construct (gRNA_{control}; Table 1). While both gRNA_{control}
222 and gRNA₃₊₄ electroporated embryos demonstrated a 459 bp fragment of the size of intact *Fmr1*
223 sequence, gRNA₃₊₄ embryos also presented a lower-size band of 260 bp (**Fig. 6B**, red arrow),
224 which reflects the deletion of ~200 bp in electroporated cells. Next, we confirmed that this

225 deletion prevents FMRP synthesis. At E6.5 (n=7 embryos), the majority of GFP⁺ cells (80%)
226 were FMRP immunoreactive in embryos electroporated with gRNA_{control} (**Fig. 6C-C'**, arrows). In
227 contrast, only 10% of GFP⁺ cells expressed FMRP following gRNA₃₊₄ expression (**Fig. 6D-D'**,
228 arrowheads; **Fig. 6E**). Finally, we confirmed that expression of gRNA_{control} and gRNA₃₊₄ plasmids
229 was confined to dA1 neurons, showing the overlapping expression of GFP with Lhx2/9 (**Fig. 6F-**
230 **H**), a specific marker for dA1/Atoh1⁺ interneurons (Bermingham et al., 2001; Gray, 2013; Kohl et
231 al., 2012).

232 *FMRP knockout induces axon growth defects.* To examine whether FMRP knockout
233 affects dA1 axonal projections, embryos were electroporated with RNA_{control} or gRNA₃₊₄ CAG
234 plasmids at E2.5 and harvested at E4.5 (n=7-10 embryos for each plasmid) and E6.5 (n=6-9
235 embryos for each plasmid). These time points encompass the period during which dA1
236 interneurons extend their axons along a well-defined dorsal-to-ventral fascicule, cross the
237 midline, and project in a parallel ventral-to-dorsal trajectory until reaching the contralateral
238 auditory nuclei anlage (Fig. 2C; Kohl et al., 2012). As expected, flat-mount views of E4.5 control
239 embryos exhibited this typical trajectory of dA1 axons that cross the midline (**Fig. 7A-A'**,
240 arrows), indicating unaffected axonal growth with gRNA_{control} expression. Observations from
241 transverse sections further demonstrated that these axons projected in a fasciculated lateral
242 bundle in the ipsilateral route and projected to the contralateral side (**Fig. 7C-C'** arrows).
243 Strikingly, many gRNA₃₊₄⁺ expressing axons did not extend toward the floor plate and showed
244 disorganized ipsilateral routes (**Fig. 7B-B'**, dashed arrows). Observations from transverse
245 sections confirmed that axons projected ventrally in a broad mediolateral pattern rather than in a
246 directional ventrolateral route as well as extended medially toward the ventricle (**Fig. 7D-E'**,
247 arrowheads). Quantitative analyses (as illustrated in Fig. 2D) revealed that the width of the
248 GFP⁺ axonal bundle, measured in the circumferential axis, was significantly greater in gRNA₃₊₄
249 electroporated embryos than the control embryos (**Fig. 7H**; non-parametric $p < 0.001$; Mann-
250 Whitney test for this and all following comparisons). In addition, the angle of individual axons in
251 relation to the mantle zone angle of the neural tube (Fig. 2D) was significantly increased
252 following FMRP knockout ($p < 0.0001$; **Fig. S8A**). This randomized axonal growth phenotype
253 persisted in E6.5 embryos (Fig. 7G, G', arrowheads) as opposed to control embryos (**Fig. 7F-F'**,
254 arrows, **7I**; $p < 0.001$), but at a significantly reduced degree as compared to E4.5 (**Fig. S8B**;
255 $p < 0.05$). To further validate the effect of FMRP knockout using the Crispr/Cas approach, we
256 designed an additional set of guide RNAs (gRNA₁ and gRNA₂) to target exon 4 of FMRP (**Fig.**
257 **S9A**). Electroporation of gRNA₁₊₂ plasmids demonstrated significant disorganized growth of NM-
258 GFP⁺ axons ($p < 0.05$; **Fig. S9B-D**) as well as loss of FMRP immunoreactivity in the

259 electroporated cells (**Fig. S9E-F**). Together, these results indicate that FMRP is required for the
260 directed growth of NM precursor axons in a tight dorsal-to-ventral fascicule.

261 In addition to the disoriented pattern of axonal growth, possibly due to axon
262 defasciculation, fewer axons crossed and progressed to the contralateral side following FMRP
263 knockout on flat-mount views of E4.5 embryos (**Fig. 7B, B'**). Observations from transverse
264 sections confirmed that fewer axons reached the level of the floor plate (**Fig. 7E**, arrows). We
265 evaluated the rate of midline crossing by calculating the ipsilateral/contralateral ratio of GFP⁺
266 axons of the same transverse section, as described in **Fig. 2D**. At E4.5, the majority of GFP⁺
267 axons crossed the midline in control embryos, while only less than half extended contralaterally
268 following FMRP knockout (**Fig. 7J**; $p<0.01$). Yet, two days later at E6.5, the majority of GFP⁺
269 axons had crossed the midline in gRNA₃₊₄ electroporated embryos (**Fig. 7G**, arrows), similar to
270 control embryos (**Fig. 7F**, arrows; **Fig. 7K**; $p=0.645$). This observation demonstrates that FMRP
271 knockout induces a delay in reaching the floor plate but maintains the ability to cross the
272 midline.

273 *FMRP knockdown induces axon growth defects.* We next examined whether a partial
274 reduction in FMRP expression affects the axonal growth pattern using a shRNA method. *Fmr1*
275 and control (scrambled) shRNAs were cloned into a transposon-based vector system with a
276 *Tol2* vector containing doxycycline (Dox) regulatory components and an EGFP reporter (Wang
277 et al., 2018), enabling Dox-dependent temporal control of gene expression. We electroporated
278 *Fmr1* and scrambled shRNA plasmids into E2.5 hindbrains, triggered shRNA expression with
279 Dox treatment immediately following the electroporation, and fixed embryos at E4.5 and E6.5
280 ($n=6-8$ embryos for each plasmid at each stage). As expected, the scrambled-shRNA group
281 exhibited the typical dA1 projecting pattern (**Fig. 8A-A', C-C', F-F'** arrows). Embryos expressing
282 *Fmr1*-shRNA, however, showed profoundly aberrant axons (**Fig. 8B, B'**, dashed-arrows), similar
283 to the FMRP knockout effect. Transverse section views confirmed that many *Fmr1*-shRNA-
284 EGFP⁺ axons projected randomly toward the ventricular zone or toward the midline in a
285 disorganized manner (**Fig. 8D-D', E-E', G-G'**, arrowheads), in high contrast to the organized and
286 directional pattern in control embryos (**Fig. 8C-C', F-F'**). The width of *Fmr1*-shRNA-GFP⁺ axons
287 was significantly larger than that of control axons at both E4.5 (**Fig. 8H**; $p<0.01$) and E6.5 (**Fig.**
288 **8I**; $p<0.05$). Nevertheless, similar to the effect of gRNA₃₊₄ expression, the degree of the axonal
289 bundle width at E6.5 was reduced as compared to E4.5 (**Fig. S8C**; $p<0.05$). Two-way ANOVA
290 analyses did not reveal a significant effect of either the type of FMRP manipulation
291 ($F(1,29)=4.127$; $p=0.052$) or the developmental stage ($F(1,29)=1.176$; $p=0.287$) on the degree of
292 FMRP deficiency induced changes in the width of the axon bundle. Different from FMRP

293 knockout, the majority of axons following shRNA-induced FMRP knockdown appeared to cross
294 the midline normally at E4.5 (Fig. 8D, E). The rate of midline crossing was not significantly
295 different between the groups at either developmental stage (Fig. 8J, K; E4.5: $p=0.2403$; E6.5:
296 $p=0.7209$). Altogether, using two loss-of-function strategies we confirmed that FMRP expression
297 in dA1 axons is required for the directional axonal growth in a defined fascicule while navigating
298 through developing brains.

299 To further determine whether loss of FMRP impairs the organized axonal growth of NM
300 precursor axons, we analyzed its effect *in vitro*. Following electroporation of gRNA_{control} or
301 gRNA₃₊₄ plasmids at E2.5 (n=12 embryos for each plasmid), hindbrains were isolated at E3.5,
302 suspended into single cells, and incubated for 5 days. The cultures contained GFP⁺ cells along
303 with non-transfected hindbrain cells (Fig. 9). To monitor the dynamics of neurite outgrowth,
304 cultures were traced by live imaging every 6 hours. Cells expressing gRNA_{control} plasmid
305 demonstrated a gradual extension and elongation of neurites (Fig. 9A, C, E, G; Movie S1).
306 Strikingly, cells expressing gRNA₃₊₄ plasmid demonstrated neurite overgrowth accompanied by
307 aberrant turning of axons and enhanced branching along the neurites and in their terminals
308 (Fig. 9B, D, F, H, I-L; Movie S2). Quantification of the results (n=6 wells for each plasmid)
309 confirmed a gradual increase in neurite branch point ($p<0.01$) and length ($p<0.001$) over time in
310 both treatments (Fig. 9M, N). Yet the values differ greatly between the groups, as indicated for
311 instance by the ~3.5 fold increase in neurite branch points and length in cells expressing
312 gRNA₃₊₄ plasmid compared to control cells at day 4. These *in vitro* results demonstrate that
313 axons tend to spread and branch more extensively in the absence of FMRP, further verifying
314 that FMRP is required to control the axonal growth behavior of NM precursors.

315

316 **FMRP deficiency induces synaptic projection errors of NM axons in NL**

317 We next determined whether FMRP is required for presynaptic targeting by assessing the
318 effects of FMRP downregulation on the pattern of synaptic connectivity of NM axons within NL.
319 We electroporated E2 embryos with *Fmr1*-shRNA or control (scrambled) shRNA into NM
320 precursors and triggered shRNA expression with Dox treatment at E8 (Fig. 10A). This late-
321 onset expression preserved earlier developmental events of NM axons before NL neurons
322 reach their final destination. During this time window, FMRP immunoreactivity was reduced 40-
323 60% in NM cell bodies as we measured previously (Wang et al., 2018).

324 We first examined embryos at E15 (n=8 embryos for scrambled-shRNA and 9 for *Fmr1*-
325 shRNA). A typical projection pattern of NM axons was seen in both groups: EGFP⁺ axons
326 arising from NM extended to both the ipsilateral and contralateral NL. In embryos expressing

327 scrambled-shRNA, NM axons were restricted to the dorsal NL ipsilaterally and ventral NL
328 contralaterally (**Fig. 10B,D**). In contrast, embryos expressing *Fmr1*-shRNA demonstrated
329 EGFP⁺ axons that projected beyond their assigned neuropil domain, extended through the cell
330 body layer, and terminated within the other domain (**Fig. 10C,E**). We measured the area
331 containing EGFP⁺ axons in each neuropil domain of the contralateral NL and calculated the
332 dorsal/ventral ratio of this measure. This ratio was low in embryos expressing scrambled-
333 shRNA, indicating a strong preference for ventral localization, and was significantly enhanced
334 following *Fmr1*-shRNA transfection ($p=0.0079$; **Fig. 10G**), demonstrating abnormal axonal
335 overshoot. This phenotype became insignificant at E19 (n=5 embryos; **Fig. 10F-G**), indicating
336 that the effect of FMRP deficiency on axon targeting is stage-dependent.

337 We next wanted to examine whether the aberrant NM axons form synapses. By dye-
338 filling individual NL neurons, we found that EGFP⁺ axons were located immediately opposite to
339 the dorsal dendrites of NL neurons (**Fig. 11A-A'**). These EGFP⁺ axons were immunoreactive to
340 synaptotagmin 2 (Sy2; **Fig. 11B-B'**), a presynaptic vesicle calcium sensor for neurotransmitter
341 release. Together, these observations demonstrate that the aberrant NM axons form synapses.

342 Finally, we examined whether FMRP knockdown altered the morphological maturation of
343 NM axonal terminals. In embryos expressing *Fmr1*-shRNA, the number of filopodia per EGFP⁺
344 terminal is 0-2 at E15, similar to control as measured from *Athoh1*-mGFP labeled terminals (**Fig.**
345 **12**; $p=0.5695$).

346

347 **Discussion**

348 Using high-specificity genetic tools in chicken embryos, we uncovered an early onset of FMRP
349 localization in developing axons of auditory neurons and demonstrated that cell autonomous
350 FMRP expression is required for orderly and timely axonal navigation and synaptic targeting *in*
351 *vivo* during discrete episodes of axon and circuit development.

352

353 **FMRP in axon navigation**

354 NM cells are born at E2-2.5 (Rubel et al., 1976). FMRP localization can be detected as early as
355 E4 in developing axons of NM precursors, demonstrating that FMRP starts localizing in distal
356 axons of NM precursors shortly after *Fmr1* gene expression and axon genesis. This finding is
357 consistent with FMRP localization in newly formed neurites of PC-12 cells (De Diego Otero et
358 al., 2002) and axon growth cones of cultured mammalian neurons (Antar et al., 2006; Hengst et
359 al., 2006; Jain and Welshhans, 2016). FMRP has also been identified in relatively mature axons
360 as a component of Fragile X granules (FXGs) in postnatal mammalian brains (Christie et al.,

361 2009; Chyung et al., 2018; Korsak et al., 2017; Shepard et al., 2020). FMRP puncta found in
362 developing NM axons resemble these FXGs in size and density (Christie et al., 2009). However,
363 the majority of FXGs in postnatal mouse brainstems contain the Fragile X related proteins
364 (FXR1P and FXR2P) but not FMRP (Chyung et al., 2018). Whether this difference reflects
365 interspecies variation or developmental stage dependency is yet to be determined.

366 Consistent with axon localization of FMRP during early development, FMRP deficiency
367 in *Atoh1*/NM precursors results in widened axonal bundles due to randomized axonal growth
368 instead of directional growing in a defined fascicule. It is known that axon fasciculation can be
369 controlled at the level of axonal growth cones (Honig et al., 1998) and/or regulated by axon
370 tension through shaft-shaft interactions (Šmít et al., 2017). Our *in vitro* results support a likely
371 involvement of growth cone behaviors as absence of FMRP in NM precursor axons leads to
372 excessively branched growth cones together with axonal overgrowth. Indeed, previous studies
373 showed that FMRP loss enhances growth cone filopodia and attenuates growth cone collapse *in*
374 *vitro* (Antar et al., 2006; Doers et al., 2014; Li et al., 2009), and these actions may involve FMRP
375 regulation of cell adhesion and axon guidance cues. For example, FMRP colocalizes with
376 *Dscam* mRNAs in cortical axons (Jain and Welshhans, 2016) and *Dscam* promotes axon
377 fasciculation in the developing optic fiber (Bruce et al., 2017). Netrin mRNAs are associated with
378 FMRP in HEK293 cells and was linked to axon extension phenotype in *dfmr1* knockout
379 *drosophila* (Kang et al., 2019). Notably, netrin has a profound role in navigating commissural
380 axons in the hindbrain and spinal cord in a tight bundle toward the midline (Moreno-Bravo et al.,
381 2019; Serafini et al., 1996; Varadarajan et al., 2017; Yung et al., 2018). [Notably, the degree of
382 the aberrant projections decreases as development proceeds. The partial recovery in the axonal
383 directionality may suggest that FMRP-deficient axons are capable to correct their growth pattern
384 with time, as shown for instance in an ascending projection connecting specific cortical layers in
385 *Fmr1* knockout mice \(Bureau et al., 2008\). Yet, to fully decipher the fate of FMRP-deficient
386 axons, advanced *in vivo* live imaging techniques will be needed to trace the behavior of
387 individual axons.](#)

388 The second phenotype we identified is a delay in axonal midline crossing. In control
389 embryos, axons of *Atoh1*/NM precursors crossed the midline at E4.5. Following FMRP
390 knockout, the axon crossing was not complete until two days later at E6.5. This phenotype may
391 be caused by a general slowing down of axon growth *in vivo*. For example, FXS neurons
392 derived from human pluripotent stem cells show reduced neurite outgrowth (Doers et al., 2014).
393 FMRP knockdown significantly reduces axonal growth of cultured mouse neurons in response
394 to nerve growth factor (Wang et al., 2015b). This slowed growth may be partially associated with

395 FMRP regulation of microtubule signaling and dynamics (Bodaleo and Gonzalez-Billault, 2016;
396 Wang et al., 2015b). Alternatively, a delay in midline crossing could be secondary to axon
397 defasciculation. In the zebrafish forebrain, axon-axon interaction (likely axon fasciculation)
398 shapes the midline kinetics of commissural axons (Bak and Fraser, 2003). Moreover,
399 overgrowth and overbranching of axons in brains of *Drosophila* FMRP mutants were reported
400 (Pan et al., 2004), consistent with our *in vitro* data in which rather than attenuation in axonal
401 growth we observed extensive neurite growth and enhanced branching points upon FMRP
402 knockout. Reduced axon fasciculation thus may negatively affect midline crossing in auditory
403 neurons. However, a delay in midline crossing was not detected following FMRP knockdown,
404 although FMRP knockdown results in similar degrees of axon defasciculation as FMRP
405 knockout. This, then, suggests that FMRP regulates multiple factors in controlling the speed of
406 axon crossing. Additional mechanisms may include suppressed expression of axon guidance
407 genes and compromised neuronal response to guidance cues following FMRP loss (Halevy et
408 al., 2015; Li et al., 2009).

409

410 **FMRP in synaptic targeting**

411 In addition to controlling axon pathfinding, FMRP is also involved in determining the pattern of
412 local axon projection in their target area. Following acute FMRP deficiency, [NM axons](#)
413 [terminate, and likely form functional synapse, on both the dorsal and ventral dendrites of the](#)
414 [same NL neurons](#). This projection pattern is expected to negatively affect the accuracy of
415 coincidence detection of NL neurons. This change can be interpreted as a compromised ability
416 of developmental axon pruning, as seen in *Drosophila* FMRP mutants (Pan et al., 2004; Tessier
417 and Broadie, 2008). Defective synaptic elimination and dendritic pruning have also been
418 observed in brains of FXS individuals and FMRP knockout mice (Comery et al., 1997; Ivanco
419 and Greenough, 2002; Jawaid et al., 2018) as well as in FMRP-reduced NM neurons (Wang et
420 al., 2018). However, there is no evidence that NM axons normally project to both dendritic
421 domains of the same NL neurons and subsequently retract from one domain (Young and Rubel,
422 1986; Rubel and Fritsch, 2002). It is therefore likely that the aberrant axon projection following
423 FMRP knockdown reflects errors in axon targeting. NM axons with less FMRP may become less
424 sensitive to guiding cues from NL neurons or local astrocytes that control the pattern of synaptic
425 distribution (Allen-Sharpley and Cramer, 2012; Korn et al., 2012; Rotschafer et al., 2016). This
426 possibility is consistent with [the localization of FMRP puncta in the distal axonal processes \(Fig.](#)
427 [5\)](#). [Although their exact relationship with synapses is yet to be determined, it is notable that](#)

428 many FMRP puncta are not in the region where synapses are located. Thus, FMRP is likely to
429 exert its axonal functions that are identified in our study without being associated with synapses.
430 Additional lines of evidence in support of FMRP regulation of axonal targeting vis growth cone
431 dynamics include the presence of abnormal protein pattern only during the period when NM
432 axons exhibit dynamic growth cones with filopodia and the normal maturation of axonal endings
433 from growth cones to bouton-like terminals independent of FMRP expression.

434 It is worth to note that axon-glia interactions may also contribute to FMRP regulation of
435 axon events, given their well-established roles in axon guidance, fasciculation, and targeting
436 (Rigby et al., 2020). Interestingly, some of the molecules that participate in a direct axon-glia
437 contact, such as NCAM and Semaphorins-Plexins (Franceschini and Barnett, 1996; Goldberg et
438 al., 2004; Keilhauer et al., 1985; Miragall et al., 1989; Moreau-Fauvarque et al., 2003;
439 Neugebauer et al., 1988; Shim et al., 2012), are known as FMRP targets in neurons (Li et al.,
440 2009; Liao et al., 2008; Menon and Mihailescu, 2007). Hence, it is possible that lack of FMRP in
441 NM axons prevents their interaction with glial cells via these proteins that in turn, leads to
442 aberrant axonal growth. Additionally, FMRP may control axonal targeting by regulating the
443 formation of axon myelination (Doll et al., 2020; Pacey et al., 2013) which influences functional
444 development of axon terminals (Berret et al., 2016; Xu et al., 2017).

445 It remains unknown whether the tonotopic organization of NM axonal projection was
446 affected by FMRP deficiency. Our manipulations affected only ~15% NM neurons that were
447 often scattered throughout the cell group, thus unable to determine the effect on the tonotopic
448 organization. Studies of *Fmr1* knockout mice demonstrated a normal tonotopic frequency
449 representation in the auditory cortex (Kim et al., 2013). However, FMRP loss diminishes the
450 developmental plasticity of this representation (Kim et al., 2013), flattens the tonotopic
451 organization of potassium channel Kv3.1b (Strumbos et al., 2010), and results in frequency-
452 specific decreases in inhibitory presynaptic structures (McCullagh et al., 2017), suggesting a
453 potential link of FMRP with specific features of tonotopic regulations.

454

455 **New insights in FXS pathogenesis**

456 Our results enhances the current understanding of FXS pathogenesis in three aspects. First, we
457 strengthen the concept that FXS neuropathology involves sensory systems. FMRP is strongly
458 expressed in the auditory system (Zorio et al., 2017) and FMRP loss alters cellular properties of
459 auditory neurons and auditory processing (reviewed in McCullagh et al., 2020). Our current and
460 previous studies (Wang et al., 2018) further demonstrate a role of FMRP in the proper
461 development of auditory connectivity. Second, we reveal a cell autonomous regulation of FMRP

462 in axon navigation. Early-onset axon localization of FMRP suggests that this regulation occurs
463 locally in axons, supporting axonal mechanisms of FXS pathology. For example, diffusion tensor
464 imaging in FXS females revealed morphological changes in white matter tracts that may reflect
465 alterations in axon density or coherence (Barnea-Goraly et al., 2003). Thus, FMRP loss-induced
466 axon defasciculation may be a mechanism that underlies this clinical phenotype. Lastly, our
467 results add to the existing literature that FMRP loss leads to substantial alterations in developing
468 brains that may be undetectable later in life. FMRP knockout mouse cortex shows alterations in
469 connection probability, axon shape, and dendritic spine length at early, but not late postnatal
470 ages (Bureau et al., 2008; Galvez and Greenough, 2005; Nimchinsky et al., 2001). Our current
471 and previous studies further show developmentally restricted dendritic and axonal alterations in
472 auditory neurons (Wang et al., 2018). The significance of these early-onset and transient
473 changes was recently highlighted in *Drosophila*, in which the requirement of FMRP for normal
474 brain function and behaviors is tightly restricted to an early developmental period (Doll and
475 Broadie, 2015; Sears and Broadie, 2018). If this holds true in vertebrates, it would suggest that
476 early axon deficits following FMRP loss may be responsible for life-long behavioral deficits in
477 FXS. Although challenging, identifying FMRP regulation of early developmental events and
478 determining how this regulation influences later circuit properties may be the beginning of a
479 deeper understanding of FXS neuropathology. The auditory brainstem circuits and the novel
480 genetic tools developed in this study provide a strategy that contributes to this effort.

481

482 **Materials and Methods**

483 **Animals and *in ovo* electroporation**

484 Fertilized White Leghorn and Loman Broiler chicken eggs (*Gallus gallus domesticus*) were
485 obtained from Charles River Laboratories (Wilmington, MA, USA) and Gil-Guy Farm (Orot,
486 Israel), respectively. Eggs were incubated for 2 to 2.5 days at 38°C until Hamburger Hamilton
487 Stage 12-15. *In ovo* electroporation was performed as described previously (Kohl et al., 2012;
488 Wang et al., 2018). Briefly, DNA constructs (4-5 µg/µl, diluted in phosphate-buffered saline
489 [PBS]) were injected into the lumen of neural tubes at the rhombomere 5-6 level.

490 Electroporation was performed with a platinum bipolar electrode or bent L-shaped gold
491 electrodes that were placed on the two sides of the hindbrain to gain unilateral transfection.
492 Embryos underwent 4 electrical pulses of 20-25 volts 30-45 ms in duration using a BTX 3000
493 (Harvard Apparatus, Cambridge, MA, USA) or a Grass SD9 electroporator (Grass instruments,
494 Quincy, MA, USA). Following electroporation, the eggs were re-incubated until dissection at
495 desired developmental stages. Embryos electroporated with drug inducible constructs (see

496 below) were treated by adding 50 μ l of doxycycline (1 mg/ml in sterile PBS; MilliporeSigma, St.
497 Louis, MO, USA) onto the chorioallantoic membrane to trigger transgene transcription.
498 Following the first Dox administration, embryos were treated again every other day to maintain
499 gene expression before tissue dissection.

500

501 **Hindbrain primary cultures and time lapse analysis**

502 Hindbrains from electroporated embryos were dissected at E3.5 and incubated for 10 minutes at
503 37°C with TrypLE Express (Gibco, Thermo Fisher Scientific, Waltham, MA, USA) to dissociate
504 the tissue into single cells, as previously described (Peretz et al., 2016; Peretz et al., 2018).
505 TrypLE was neutralized with embryonic stem cell media containing DMEM/F-12 1:1, 20%
506 KnockOut serum replacement, 2 μ M GlutaMax L-alanyl-L-glutamine, 0.1 μ M nonessential
507 amino acids, and 1:50 penicillin-streptomycin (all from Gibco, Thermo Fisher Scientific),
508 together with 0.1 μ M β -mercaptoethanol and amphotericin B (1:400) (both from
509 MilliporeSigma). Cells were passed through a 100 μ m mesh strainer, centrifuged at 600 g for 10
510 minutes, seeded in 48-well plates ($\sim 2 \times 10^5$ cells/well) (Nunclon Delta Surface, Thermo Fisher
511 Scientific), and incubated at 37°C in 5% CO₂. For live imaging, well plates were imaged every 6
512 hours in the IncuCyte S3 Zoom HD/2CLR time-lapse microscopy system equipped with x
513 20_Plan Fluorobjective (Sartorius, Göttingen, Germany). Time-lapse movies were generated by
514 capturing phase and green fluorescence images of cells in wells for up to 5 days. Stacks of
515 images were exported in TIF format using the IncuCyte graph/export menu. Videos were
516 assembled by exporting into MP4 format.

517

518 **Plasmid construction**

519 For genetic targeting of Atoh1 neurons, an Atoh1-enhancer element (Helms et al., 2000;
520 Pennacchio et al., 2006) was cloned upstream to a Cre-recombinase sequence (Atoh1-Cre) and
521 electroporated along with a conditional reporter plasmid containing a floxed STOP cassette in
522 between the CAGG enhancer/promoter module and nuclear (n) or membranal (m) *GFP* gene
523 (pCAGG-LoxP-STOP-LoxP-n/mGFP), as previously reported (Avraham et al., 2009; Kohl et al.,
524 2012; Lumpkin et al., 2003; Reeber et al., 2008). For plasmid integration into the genome, the
525 conditional reporter cassette was cloned between two PiggyBac (PB) arms (PB-CAGG-LoxP-
526 STOPLoxPSTOP-GFP-PB) and electroporated along with the Atoh1-Cre and Pbase
527 transposase plasmids (Hadas et al., 2014; Kohl et al., 2012; Lu et al., 2009; Wang et al., 2010).
528 For tracing pre-synaptic connections, a reporter plasmid containing the synaptic tracer SV2-

529 GFP (PB-CAG-LoxP-STOP-LoxP-SV2- GFP-PB) (Hadas et al., 2014; Kohl et al., 2012) was
530 electroporated along with the Atoh1 enhancer and the Pbase transposase.

531 For constitutive expression of chicken or human *Fmr1*, mCherry-*Fmr1* fused coding
532 sequence was chemically synthesized (GenScript, Piscataway, NJ) and sub-cloned into the
533 pT2K-CAGGS vector. For electroporation, the two plasmids (pT2K-CAGGS-mCherry-chFMRP
534 and pCAGGS-T2TP) were concentrated at 4-5 µg/µl and mixed at equal amounts.

535 For shRNA targeting of FMRP, five shRNAs directed against specific sequences of
536 chicken *Fmr1* were designed using siRNA Wizard v3.1 (InvivoGen, San Diego, CA, USA) and
537 the siDESIGN Center (Thermo Fisher Scientific). Plasmids were chemically synthesized
538 (GENEWIZ, South Plainfield, NJ, USA) and endo free DNA Maxi Preps were performed
539 (Qiagen, Hilden, Germany). The most effective shRNA (gaggatcaagatgcagtgaata; nucleotides
540 951-973 of chicken *Fmr1*) was determined based on its knockdown effect in the developing
541 brainstem (Wang et al., 2018) and used for subsequent experiments. A scrambled shRNA
542 (attagaataagtgcgagagaata) was designed using the Genscript algorithm (Piscataway, NJ, USA)
543 and confirmed by blasting this shRNA sequence against the chicken genome. *Fmr1* and
544 scrambled shRNAs were cloned into a transposon-based vector system with a *Tol2* vector
545 containing doxycycline regulatory components (Schecterson et al., 2012; Wang et al., 2018).
546 *Tol2* transposable element sequences enable stable integration of the transposon into the chick
547 genome, whereas doxycycline regulatory elements allow temporal control of gene expression.

548 For Crispr/Cas9 targeting of FMRP, we used the Genome Engineering Toolbox that was
549 designed by the Zhang lab (Cong et al., 2013). The pX330 plasmid (addgene) (Sakuma et al.,
550 2014) was modified by adding a T2A-EGFP cassette at the carboxyl terminus of Cas9. gRNAs
551 to *Fmr1* were designed utilizing the chopchop design tool (<https://chopchop.cbu.uib.no/>). gRNAs
552 targeting exon 8 were cloned into the modified pX330 plasmid (Table 1). For testing the
553 efficiency of the gRNA, the targeting plasmids were electroporated into the hindbrain at E2.5.
554 Hindbrains were dissected 48 hours following electroporation, and a 2 mm hindbrain tissue was
555 processed for DNA extraction, using 'tail digestion and DNA extraction' protocol (Wang and
556 Storm, 2006). Genomic DNA was analyzed by polymerase chain reaction (PCR) using primers
557 specific to sequences up- and down-stream of the FMRP-gRNA₃₊₄ target sites. Nested PCR
558 was used to amplify the targeted region. For exon 8 targeting, Test-F3 and Test-R1 were used
559 for the first round of PCR, followed by Test-F2 and Test-R2 for the second round.

560

	Exon of <i>Fmr1</i>	
G3	Exon8	GAGGTGGACCAACTACGTT

G4	Exon8	ACGTGGTCCAGGCTACGCTT
control		GGGTCTTCGAGAAGACCTG
Test-F3	Exon8	AGGTTGCTACCAGCTGTTGG
Test-F4	Exon8	TACTGCTATGAATAGCTCCTG
Test-R1	Exon8	GAAGCTATGTGCAAATATTAGCAG
Test-R2	Exon8	TTCTCATTGAACACTTGCATTTC

Table 1. Plasmid sequences for gRNA production and validation.

561

562

563 **Staining and immunocytochemistry**

564 Brainstem was dissected at various stages and immersed in 4% paraformaldehyde in 0.1 M
565 phosphate buffer (PB) overnight at 4°C. For whole mount preparation, hindbrains were cut open
566 along the roof plate, after which the tissue was spread open on slides to produce flat-mount
567 preparations (Kayam et al., 2013; Weisinger et al., 2012). For transverse sections, brainstems
568 were transferred to 30% sucrose in PB until settling, followed by their sectioning in the coronal
569 plane at 30 µm. Alternate sections were immunohistochemically stained by incubation with
570 primary antibody solutions diluted in PBS with 0.3% Triton X-100 overnight at 4°C, followed by
571 Alexa-Fluor secondary antibodies (Life Technologies, Carlsbad, CA, USA) at 1:1000 overnight
572 at 4°C. Some sections were counterstained with DAPI and/or NeuroTrace (Life Technologies), a
573 fluorescent Nissl stain, at a concentration of 1:1000 and incubated together with secondary
574 antibodies. Sections were mounted on gelatin-coated slides and coverslipped with Fluoromount-
575 G mounting medium[®] (Southern Biotech, Birmingham, AL, USA) for imaging.

576 Primary antibodies used include the custom-made polyclonal rabbit anti-FMRP (Wang et
577 al., 2018; Yu et al., 2020), anti-Synaptotagmin 2 (1:1000, DSHB Cat# znp-1, RRID:
578 AB_2315626), anti-SNAP25 (1:1000, Abcam Cat# 5666, RRID: AB_305033), anti-microtubule
579 associated protein 2 (MAP2; Milipore, Burlington, MA, USA; #MAB 3418; RRID: AB_94856),
580 custom-made polyclonal rabbit anti-Lhx2/9 (1:100, [I. Sibony and T.Schultheiss, unpublished](#)
581 [data; kind gift from T. Schultheiss, Technion-Israel Institute of Technology, Haifa, Israel](#)), and
582 polyclonal rabbit anti VGlut2 (1:150, Synaptic Systems, Göttingen, Germany; CAT# 135402.)

583

584 **Single-cell filling**

585 [Following electroporation with *Fmr1*-shRNA plasmids and doxycycline treatment, E15 embryos](#)
586 [were used to prepare acute brainstem slices as previously described \(Wang et al., 2017\). NL](#)

587 cells were individually dye-filled with Alexa Fluoro 568 dextran (Invitrogen) following our
588 published protocol (Wang and Rubel, 2012; Wang et al., 2017).

589

590 **Data analysis**

591 Quantification of Atoh1-Cre NM ratio. Atoh1-Cre transfected NM neurons and total NM neurons
592 counterstained by NeuroTrace on each section were counted using Cell Counter of Image J.
593 Sections from the same animal were grouped, and the transfection ratio was calculated as:
594 transfection ratio = number of Atoh1-mGFP⁺ NM neurons / total NM neurons (n=8 embryos).

595 Quantification of axon terminal morphology. The axon terminal morphology was
596 characterized by numbers of filopodia. Image stacks containing identifiable intact axon terminals
597 were reconstructed using image J, and the numbers of filopodia on each terminal were counted
598 on both ipsilateral and contralateral sides. Number of filopodium per terminal was then
599 calculated and compared between the immature stages (E11-E13) and E15.

600 Localization analysis of FMRP granule. FMRP granules localization in Atoh1-mGFP
601 labeled axons were analyzed using Image J. Briefly, a straight-line ROI was drawn across a
602 FMRP granule with Atoh1-mGFP transfection and applied to both channels respectively. The
603 fluorescent intensity profile was then analyzed and plotted using GraphPad Prism 7 software.

604 Quantification of gRNA expressing cells. Quantification of expression of gRNA_{control} and gRNA₃₊₄
605 plasmids in dA1 cells is demonstrated by Box plot analysis. For each group, two transverse
606 sections obtained from 3 different embryos at E4.5 were taken. Each data point represents one
607 section. The ratio of cells that co-express gRNA-GFP⁺ and the dA1-specific marker Lhx2/9 out
608 of the total gRNA-GFP⁺ expressing cells is presented.

609 Quantification of FMRP expression. Quantification of the extent of FMRP expression in
610 gRNA_{control} and gRNA₃₊₄ expressing cells is demonstrated by Box plot analysis. For each group,
611 electroporated sagittal sections obtained from 7 different embryos at E6 were taken. Each data
612 point represents one section for which the ratio of (FMRP⁺+GFP⁺)/GFP⁺ cells was measured.

613 Quantification of gRNA expressing cells. Quantification of expression of gRNA_{control} and
614 gRNA₃₊₄ plasmids in dA1 cells is demonstrated by Box plot analysis. For each group, two
615 transverse sections obtained from 3 different embryos at E4.5 were taken. Each data point
616 represents one section. The ratio of cells that co-express gRNA-GFP⁺ and the dA1-specific
617 marker Lhx2/9 out of the total gRNA-GFP⁺ expressing cells is presented.

618 Quantification of axon fascicule width. Axonal width measurement was performed for 2
619 different experiments (Fmr1-shRNA and FMRP-Crispr) at E4.5 and E6.5. Each stage included 2
620 groups: (1) gRNA_{control} and gRNA₃₊₄ expressing cells and (2) sc-shRNA-GFP and Fmr1-shRNA-

621 GFP expressing cells. Box plots are demonstrated for each group, from which cross sections
622 from 7 different embryos (E4.5) or 4 embryos (E6.5) were taken. Each data point represents
623 one section for which the ratio of the axonal length related to the mantle-ventricular width was
624 measured using ImageJ software.

625 Quantification of axonal crossing. Box plot quantification of axonal crossing was
626 performed for 2 different experiments at E4.5 and E6.5. Each stage contained 2 groups: (1)
627 gRNA_{control} and gRNA₃₊₄ expressing cells and (2) sc-shRNA-GFP and FMR1-shRNA-GFP
628 expressing cells. For each group, cross sections from 7 different embryos (E4.5) or 4 embryos
629 (E6.5) were taken. Each data point represents one section for which the ratio of the signal
630 intensity between commissural axons and non-commissural axons was measured using ImageJ
631 software.

632 Quantification of neurite length and branch points in cultures. Neurite length (mm/mm²)
633 and branch point (per mm²) were calculated in gRNA_{control} and gRNA₃₊₄ expressing neurons in
634 each well (n=6 wells for each treatment) using the IncuCyte Zoom NeuroTrack software module
635 (Sartorius, USA), as described in (Wurster et al., 2019). Microplate graphs were generated
636 using the time plot feature in the graph/export menu of the IncuCyte Zoom software.

637 Quantification of Atoh1-Cre expressing cells. Percentage of Atoh1-Cre::nGFP expressing cells
638 was calculated by counting the number of GFP⁺ nuclei that co-express the dA1-specific marker
639 Lhx2/9 out of the total GFP-expressing nuclei (n=7 embryos).

640 Quantification of the laminar specificity of axon targeting. Axonal projection was
641 measured from Fmr1-shRNA transfected embryos at E15 and E19, as well as from scrambled-
642 shRNA transfected embryos at E15 using Image J. For each embryo, transverse sections
643 containing the middle and rostral NL where NL cell bodies are aligned into a single layer were
644 used for the analysis. For each section, the dorsal and ventral neuropil regions of NL on the side
645 contralateral to the transfection were outlined based on NeuroTrace staining. The neuropil area
646 covered by EGFP⁺ axons was then measured for each neuropil region. The specificity of axon
647 projection was evaluated by calculating the ratio of the dorsal EGFP⁺ area to the ventral EGFP⁺
648 area. The ratios from all sections (usually 2-3) of the same embryo were averaged as individual
649 data points and compared between Fmr1-shRNA and control-shRNA transfected animals (n=5-
650 9 animals for each group).

651 Statistics. Statistics were performed by Mann-Whitney non-parametric test using the
652 Graphpad Prism 7 software package (GraphPad Software, La Jolla, CA, USA). $p < 0.05$ was
653 considered statistically significant. Data were displayed as mean \pm SD or SEM as indicated in

654 the Results. Each individual data point represents one animal. Two-way ANOVA was used for
655 Tukey multiple comparisons.

656

657 **Acknowledgements**

658 We thank Edwin W Rubel (University of Washington) for facilitating the collaboration between
659 YW and DSD. We are grateful to David Fradkin for his assistance with the IncuCyte system,
660 [Itzhak Sibony](#) and Tom Schultheiss for the Lhx2/9 antibody, and Daniel Lazar for her help with the
661 tissue culture.

662

663 **Competing interests**

664 No competing interests declared.

665

666 **Funding**

667 This work was supported by the National Institutes of Health (DC13074 and DC17267 to Y. W.),
668 the United States – Israel Binational Science Foundation (2015087 to Y.W. and D.S.), The
669 Israel Science Foundation (1515/16 to D.S) and The [Chief Scientist Office, Ministry of Health \(3-
670 0000-33793 to D.S\)](#).

671

672 **Data Availability**

673 None.

674

675 **References**

676 Abitbol, M., Menini, C., Delezoide, A. L., Rhyner, T., Vekemans, M. and Mallet, J. (1993).

677 Nucleus basalis magnocellularis and hippocampus are the major sites of FMR-1

678 expression in the human fetal brain. *Nat. Genet.* 4, 147–153.

679 Allen-Sharpley, M. R. and Cramer, K. S. (2012). Coordinated Eph-ephrin signaling guides

680 migration and axon targeting in the avian auditory system. *Neural Dev* 7, 29.

681 Antar, L. N., Li, C., Zhang, H., Carroll, R. C. and Bassell, G. J. (2006). Local functions for FMRP

682 in axon growth cone motility and activity-dependent regulation of filopodia and spine

683 synapses. *Molecular and Cellular Neuroscience* 32, 37–48.

684 Avraham, O., Hadas, Y., Vald, L., Zisman, S., Schejter, A., Visel, A. and Avihu, K. (2009).

685 Transcriptional control of axonal guidance and sorting in dorsal interneurons by the Lim-

686 HD proteins Lhx9 and Lhx1. *Neural Dev* 4, 21.

687 Bagni, C. and Greenough, W. T. (2005). From mRNP trafficking to spine dysmorphogenesis: the
688 roots of fragile X syndrome. *Nat. Rev. Neurosci.* 6, 376–387.

689 Bagni, C. and Zukin, R. S. (2019). A Synaptic Perspective of Fragile X Syndrome and Autism
690 Spectrum Disorders. *Neuron* 101, 1070–1088.

691 Bak, M. and Fraser, S. E. (2003). Axon fasciculation and differences in midline kinetics between
692 pioneer and follower axons within commissural fascicles. *Development* 130, 4999–5008.

693 Barnea-Goraly, N., Eliez, S., Hedeus, M., Menon, V., White, C. D., Moseley, M. and Reiss, A. L.
694 (2003). White matter tract alterations in fragile X syndrome: Preliminary evidence from
695 diffusion tensor imaging. *Am. J. Med. Genet.* 118B, 81–88.

696 Bassell, G. J. and Warren, S. T. (2008). Fragile X Syndrome: Loss of Local mRNA Regulation
697 Alters Synaptic Development and Function. *Neuron* 60, 201–214.

698 Bear, M. F., Huber, K. M. and Warren, S. T. (2004). The mGluR theory of fragile X mental
699 retardation. *Trends Neurosci.* 27, 370–377.

700 Bermingham, N. A., Hassan, B. A., Wang, V. Y., Fernandez, M., Banfi, S., Bellen, H. J.,
701 Fritsch, B. and Zoghbi, H. Y. (2001). Proprioceptor pathway development is dependent
702 on Math1. *Neuron* 30, 411–422.

703 Berret, E., Kim, S. E., Lee, S. Y., Kushmerick, C. and Kim, J. H. (2016). Functional and
704 structural properties of ion channels at the nerve terminal depends on compact myelin:
705 Ion channels at the CNS nerve terminal. *J. Physiol.* 594, 5593–5609.

706 Bodaleo, F. J. and Gonzalez-Billault, C. (2016). The Presynaptic Microtubule Cytoskeleton in
707 Physiological and Pathological Conditions: Lessons from Drosophila Fragile X Syndrome
708 and Hereditary Spastic Paraplegias. *Front Mol Neurosci* 9, 60.

709 Brown, M. R., Kronengold, J., Gazula, V.-R., Chen, Y., Strumbos, J. G., Sigworth, F. J.,
710 Navaratnam, D. and Kaczmarek, L. K. (2010). Fragile X mental retardation protein
711 controls gating of the sodium-activated potassium channel Slack. *Nat Neurosci* 13, 819–
712 821.

713 Bruce, F. M., Brown, S., Smith, J. N., Fuerst, P. G. and Erskine, L. (2017). DSCAM promotes
714 axon fasciculation and growth in the developing optic pathway. *Proc. Natl. Acad. Sci.*
715 *U.S.A.* 114, 1702–1707.

716 Bureau, I., Shepherd, G. M. G. and Svoboda, K. (2008). Circuit and Plasticity Defects in the
717 Developing Somatosensory Cortex of Fmr1 Knock-Out Mice. *Journal of Neuroscience*
718 28, 5178–5188.

719 Castrén, M. L. (2016). Cortical neurogenesis in fragile X syndrome. *Front Biosci* 8, 160–168.

720 Chédotal, A. and Richards, L. J. (2010). Wiring the Brain: The Biology of Neuronal Guidance.
721 *Cold Spring Harbor Perspectives in Biology* 2, a001917–a001917.

722 Christie, S. B., Akins, M. R., Schwob, J. E. and Fallon, J. R. (2009). The FXG: a presynaptic
723 fragile X granule expressed in a subset of developing brain circuits. *J. Neurosci.* 29,
724 1514–1524.

725 Chyung, E., LeBlanc, H. F., Fallon, J. R. and Akins, M. R. (2018). Fragile X granules are a
726 family of axonal ribonucleoprotein particles with circuit-dependent protein composition
727 and mRNA cargos. *J Comp Neurol* 526, 96–108.

728 Comer, J. D., Alvarez, S., Butler, S. J. and Kaltschmidt, J. A. (2019). Commissural axon
729 guidance in the developing spinal cord: from Cajal to the present day. *Neural Dev* 14, 9.

730 Comery, T. A., Harris, J. B., Willems, P. J., Oostra, B. A., Irwin, S. A., Weiler, I. J. and
731 Greenough, W. T. (1997). Abnormal dendritic spines in fragile X knockout mice:
732 maturation and pruning deficits. *Proc. Natl. Acad. Sci. U.S.A.* 94, 5401–5404.

733 Cong, L., Ran, F. A., Cox, D., Lin, S., Barretto, R., Habib, N., Hsu, P. D., Wu, X., Jiang, W.,
734 Marraffini, L. A., et al. (2013). Multiplex genome engineering using CRISPR/Cas
735 systems. *Science* 339, 819–823.

736 Cramer, K. S., Fraser, S. E. and Rubel, E. W. (2000). Embryonic Origins of Auditory Brain-Stem
737 Nuclei in the Chick Hindbrain. *Developmental Biology* 224, 138–151.

738 Cramer, K. S., Bermingham-McDonogh, O., Krull, C. E. and Rubel, E. W. (2004). EphA4
739 signaling promotes axon segregation in the developing auditory system. *Developmental*
740 *Biology* 269, 26–35.

741 Davis, J. K. and Broadie, K. (2017). Multifarious Functions of the Fragile X Mental Retardation
742 Protein. *Trends Genet.* 33, 703–714.

743 [De Diego Otero, Y., Severijnen, L.-A., van Cappellen, G., Schrier, M., Oostra, B. and Willemsen,](#)
744 [R. \(2002\). Transport of fragile X mental retardation protein via granules in neurites of](#)
745 [PC12 cells. *Mol. Cell. Biol.* 22, 8332–8341.](#)

746 Deng, P.-Y., Rotman, Z., Blundon, J. A., Cho, Y., Cui, J., Cavalli, V., Zakharenko, S. S. and
747 Klyachko, V. A. (2013). FMRP regulates neurotransmitter release and synaptic
748 information transmission by modulating action potential duration via BK channels.
749 *Neuron* 77, 696–711.

750 Doers, M. E., Musser, M. T., Nichol, R., Berndt, E. R., Baker, M., Gomez, T. M., Zhang, S.-C.,
751 Abbeduto, L. and Bhattacharyya, A. (2014). iPSC-derived forebrain neurons from FXS
752 individuals show defects in initial neurite outgrowth. *Stem Cells Dev.* 23, 1777–1787.

753 Doll, C. A. and Broadie, K. (2015). Activity-dependent FMRP requirements in development of
754 the neural circuitry of learning and memory. *Development* 142, 1346–1356.

755 Doll, C. A., Yergert, K. M. and Appel, B. H. (2020). The RNA binding protein fragile X mental
756 retardation protein promotes myelin sheath growth. *Glia* 68, 495–508.

757 El-Hassar, L., Song, L., Tan, W. J. T., Large, C. H., Alvaro, G., Santos-Sacchi, J. and
758 Kaczmarek, L. K. (2019). Modulators of Kv3 Potassium Channels Rescue the Auditory
759 Function of Fragile X Mice. *J. Neurosci.* 39, 4797–4813.

760 Farago, A. F., Awatramani, R. B. and Dymecki, S. M. (2006). Assembly of the Brainstem
761 Cochlear Nuclear Complex Is Revealed by Intersectional and Subtractive Genetic Fate
762 Maps. *Neuron* 50, 205–218.

763 Farzin, F., Rivera, S. M. and Whitney, D. (2011). Resolution of spatial and temporal visual
764 attention in infants with fragile X syndrome. *Brain* 134, 3355–3368.

765 Ferron, L., Nieto-Rostro, M., Cassidy, J. S. and Dolphin, A. C. (2014). Fragile X mental
766 retardation protein controls synaptic vesicle exocytosis by modulating N-type calcium
767 channel density. *Nat Commun* 5, 3628.

768 [Franceschini, I. A. and Barnett, S. C. \(1996\). Low-affinity NGF-receptor and E-N-CAM
769 expression define two types of olfactory nerve ensheathing cells that share a common
770 lineage. *Dev. Biol.* 173, 327–343.](#)

771 Fujiyama, T., Yamada, M., Terao, M., Terashima, T., Hioki, H., Inoue, Y. U., Inoue, T.,
772 Masuyama, N., Obata, K., Yanagawa, Y., et al. (2009). Inhibitory and excitatory
773 subtypes of cochlear nucleus neurons are defined by distinct bHLH transcription factors,
774 Ptf1a and Atoh1. *Development* 136, 2049–2058.

775 Galvez, R. and Greenough, W. T. (2005). Sequence of abnormal dendritic spine development in
776 primary somatosensory cortex of a mouse model of the fragile X mental retardation
777 syndrome. *Am. J. Med. Genet. A* 135, 155–160.

778 Garcia-Pino, E., Gessele, N. and Koch, U. (2017). Enhanced Excitatory Connectivity and
779 Disturbed Sound Processing in the Auditory Brainstem of Fragile X Mice. *J. Neurosci.*
780 [37, 7403–7419.](#)

781 [Goldberg, J. L., Vargas, M. E., Wang, J. T., Mandemakers, W., Oster, S. F., Sretavan, D. W.
782 and Barres, B. A. \(2004\). An oligodendrocyte lineage-specific semaphorin, Sema5A,
783 inhibits axon growth by retinal ganglion cells. *J. Neurosci.* 24, 4989–4999.](#)

784 Gray, P. A. (2013). Transcription factors define the neuroanatomical organization of the
785 medullary reticular formation. *Front Neuroanat* 7, 7.

786 Hadas, Y., Etlin, A., Falk, H., Avraham, O., Kobilier, O., Panet, A., Lev-Tov, A. and Klar, A.
787 (2014). A 'tool box' for deciphering neuronal circuits in the developing chick spinal cord.
788 *Nucleic Acids Research* 42, e148–e148.

789 Hagerman, R. J., Berry-Kravis, E., Hazlett, H. C., Bailey, D. B., Moine, H., Kooy, R. F., Tassone,
790 F., Gantois, I., Sonenberg, N., Mandel, J. L., et al. (2017). Fragile X syndrome. *Nat Rev*
791 *Dis Primers* 3, 17065.

792 Halevy, T., Czech, C. and Benvenisty, N. (2015). Molecular mechanisms regulating the defects
793 in fragile X syndrome neurons derived from human pluripotent stem cells. *Stem Cell*
794 *Reports* 4, 37–46.

795 Hall, S. S., Walter, E., Sherman, E., Hoeft, F. and Reiss, A. L. (2009). The neural basis of
796 auditory temporal discrimination in girls with fragile X syndrome. *J Neurodevelop Disord*
797 1, 91–99.

798 Helms, A. W., Abney, A. L., Ben-Arie, N., Zoghbi, H. Y. and Johnson, J. E. (2000).
799 Autoregulation and multiple enhancers control Math1 expression in the developing
800 nervous system. *Development* 127, 1185–1196.

801 Hendricks, S. J., Rubel, E. W. and Nishi, R. (2006). Formation of the avian nucleus
802 magnocellularis from the auditory anlage. *J. Comp. Neurol.* 498, 433–442.

803 Hengst, U., Cox, L. J., Macosko, E. Z. and Jaffrey, S. R. (2006). Functional and selective RNA
804 interference in developing axons and growth cones. *J. Neurosci.* 26, 5727–5732.

805 Hille, F. and Charpentier, E. (2016). CRISPR-Cas: biology, mechanisms and relevance. *Phil.*
806 *Trans. R. Soc. B* 371, 20150496.

807 Hinds, H. L., Ashley, C. T., Sutcliffe, J. S., Nelson, D. L., Warren, S. T., Housman, D. E. and
808 Schalling, M. (1993). Tissue specific expression of FMR-1 provides evidence for a
809 functional role in fragile X syndrome. *Nat. Genet.* 3, 36–43.

810 Honig, M. G., Petersen, G. G., Rutishauser, U. S. and Camilli, S. J. (1998). In vitro studies of
811 growth cone behavior support a role for fasciculation mediated by cell adhesion
812 molecules in sensory axon guidance during development. *Dev. Biol.* 204, 317–326.

813 Ivanco, T. L. and Greenough, W. T. (2002). Altered mossy fiber distributions in adultFmr1 (FVB)
814 knockout mice. *Hippocampus* 12, 47–54.

815 Jain, S. and Welshhans, K. (2016). Netrin-1 induces local translation of down syndrome cell
816 adhesion molecule in axonal growth cones: Local Translation of Dscam. *Devel Neurobio*
817 76, 799–816.

818 Jawaid, S., Kidd, G. J., Wang, J., Swetlik, C., Dutta, R. and Trapp, B. D. (2018). Alterations in
819 CA1 hippocampal synapses in a mouse model of fragile X syndrome. *Glia* 66, 789–800.

820 Kang, H., Zhao, J., Jiang, X., Li, G., Huang, W., Cheng, H. and Duan, R. (2019). *Drosophila*
821 Netrin-B controls mushroom body axon extension and regulates courtship-associated
822 learning and memory of a *Drosophila fragile X syndrome* model. *Mol Brain* 12, 52.

823 Kayam, G., Kohl, A., Magen, Z., Peretz, Y., Weisinger, K., Bar, A., Novikov, O., Brodski, C. and
824 Sela-Donenfeld, D. (2013). A novel role for Pax6 in the segmental organization of the
825 hindbrain. *Development* 140, 2190–2202.

826 Keilhauer, G., Faissner, A. and Schachner, M. (1985). Differential inhibition of neurone-neurone,
827 neurone-astrocyte and astrocyte-astrocyte adhesion by L1, L2 and N-CAM antibodies.
828 *Nature* 316, 728–730.

829 Kéri, S. and Benedek, G. (2011). Fragile X protein expression is linked to visual functions in
830 healthy male volunteers. *Neuroscience* 192, 345–350.

831 Kim, H., Gibboni, R., Kirkhart, C. and Bao, S. (2013). Impaired critical period plasticity in primary
832 auditory cortex of fragile X model mice. *J. Neurosci.* 33, 15686–15692.

833 Kogan, C. S., Bertone, A., Cornish, K., Boutet, I., Der Kaloustian, V. M., Andermann, E.,
834 Faubert, J. and Chaudhuri, A. (2004). Integrative cortical dysfunction and pervasive
835 motion perception deficit in fragile X syndrome. *Neurology* 63, 1634–1639.

836 Kohl, A., Hadas, Y., Klar, A. and Sela-Donenfeld, D. (2012). Axonal Patterns and Targets of dA1
837 Interneurons in the Chick Hindbrain. *Journal of Neuroscience* 32, 5757–5771.

838 Kohl, A., Hadas, Y., Klar, A. and Sela-Donenfeld, D. (2013). Electroporation of the Hindbrain to
839 Trace Axonal Trajectories and Synaptic Targets in the Chick Embryo. *JoVE* 50136.

840 Kohl, A., Marquardt, T., Klar, A. and Sela-Donenfeld, D. (2015). Control of Axon Guidance and
841 Neurotransmitter Phenotype of dB1 Hindbrain Interneurons by Lim-HD Code. *Journal of*
842 *Neuroscience* 35, 2596–2611.

843 Korn, M. J., Koppel, S. J., Li, L. H., Mehta, D., Mehta, S. B., Seidl, A. H. and Cramer, K. S.
844 (2012). Astrocyte-secreted factors modulate the developmental distribution of inhibitory
845 synapses in nucleus laminaris of the avian auditory brainstem. *J. Comp. Neurol.* 520,
846 1262–1277.

847 Korsak, L. I. T., Shepard, K. A. and Akins, M. R. (2017). Cell type-dependent axonal localization
848 of translational regulators and mRNA in mouse peripheral olfactory neurons. *J Comp*
849 *Neurol* 525, 2202–2215.

850 Li, C., Bassell, G. and Sasaki, Y. (2009). Fragile X Mental Retardation Protein is involved in
851 protein synthesis-dependent collapse of growth cones induced by Semaphorin-3A.
852 *Front. Neural Circuits* 3,.

853 [Liao, L., Park, S. K., Xu, T., Vanderklish, P. and Yates, J. R. \(2008\). Quantitative proteomic](#)
854 [analysis of primary neurons reveals diverse changes in synaptic protein content in *fmr1*](#)
855 [knockout mice. *PNAS* 105, 15281–15286.](#)

856 Lipovsek, M. and Wingate, R. J. (2018). Conserved and divergent development of brainstem
857 vestibular and auditory nuclei. *eLife* 7, e40232.

858 Lu, Y. (2019). Subtle differences in synaptic transmission in medial nucleus of trapezoid body
859 neurons between wild-type and *Fmr1* knockout mice. *Brain Research* 1717, 95–103.

860 Lu, Y., Lin, C. and Wang, X. (2009). PiggyBac transgenic strategies in the developing chicken
861 spinal cord. *Nucleic Acids Res.* 37, e141.

862 Lumpkin, E. A., Collisson, T., Parab, P., Omer-Abdalla, A., Haeberle, H., Chen, P., Doetzlhofer,
863 A., White, P., Groves, A., Segil, N., et al. (2003). Math1-driven GFP expression in the
864 developing nervous system of transgenic mice. *Gene Expr. Patterns* 3, 389–395.

865 Machold, R. and Fishell, G. (2005). Math1 Is Expressed in Temporally Discrete Pools of
866 Cerebellar Rhombic-Lip Neural Progenitors. *Neuron* 48, 17–24.

867 Maricich, S. M., Xia, A., Mathes, E. L., Wang, V. Y., Oghalai, J. S., Fritsch, B. and Zoghbi, H.
868 Y. (2009). Atoh1-Lineal Neurons Are Required for Hearing and for the Survival of
869 Neurons in the Spiral Ganglion and Brainstem Accessory Auditory Nuclei. *Journal of*
870 *Neuroscience* 29, 11123–11133.

871 [McCullagh, E. A., Salcedo, E., Huntsman, M. M. and Klug, A. \(2017\). Tonotopic alterations in](#)
872 [inhibitory input to the medial nucleus of the trapezoid body in a mouse model of Fragile](#)
873 [X syndrome. *J Comp Neurol* 525, 3543–3562.](#)

874 [McCullagh, E. A., Rotschafer, S. E., Auerbach, B. D., Klug, A., Kaczmarek, L. K., Cramer, K. S.,](#)
875 [Kulesza, R. J., Razak, K. A., Lovelace, J. W., Lu, Y., et al. \(2020\). Mechanisms](#)
876 [underlying auditory processing deficits in Fragile X syndrome. *FASEB J.*](#)

877 Menon, L. and Mihailescu, M.-R. (2007). Interactions of the G quartet forming semaphorin 3F
878 RNA with the RGG box domain of the fragile X protein family. *Nucleic Acids Res.* 35,
879 5379–5392.

880 Miragall, F., Kadmon, G. and Schachner, M. (1989). Expression of L1 and N-CAM cell adhesion
881 molecules during development of the mouse olfactory system. *Dev. Biol.* 135, 272–286.

882 Moreau-Fauvarque, C., Kumanogoh, A., Camand, E., Jaillard, C., Barbin, G., Boquet, I., Love,
883 C., Jones, E. Y., Kikutani, H., Lubetzki, C., et al. (2003). The transmembrane
884 semaphorin Sema4D/CD100, an inhibitor of axonal growth, is expressed on
885 oligodendrocytes and upregulated after CNS lesion. *J. Neurosci.* 23, 9229–9239.

886 Moreno-Bravo, J. A., Roig Puiggros, S., Mehlen, P. and Chédotal, A. (2019). Synergistic Activity
887 of Floor-Plate- and Ventricular-Zone-Derived Netrin-1 in Spinal Cord Commissural Axon
888 Guidance. *Neuron* 101, 625-634.e3.

889 [Neugebauer, K. M., Tomaselli, K. J., Lilien, J. and Reichardt, L. F. \(1988\). N-cadherin, NCAM,
890 and integrins promote retinal neurite outgrowth on astrocytes in vitro. *J. Cell Biol.* 107,
891 1177–1187.](#)

892 Nimchinsky, E. A., Oberlander, A. M. and Svoboda, K. (2001). Abnormal development of
893 dendritic spines in FMR1 knock-out mice. *J. Neurosci.* 21, 5139–5146.

894 Nothwang, H. G. (2016). Evolution of mammalian sound localization circuits: A developmental
895 perspective. *Progress in Neurobiology* 141, 1–24.

896 Overholt, E. M., Rubel, E. W. and Hyson, R. L. (1992). A circuit for coding interaural time
897 differences in the chick brainstem. *J. Neurosci.* 12, 1698–1708.

898 Pacey, L. K. K., Xuan, I. C. Y., Guan, S., Sussman, D., Henkelman, R. M., Chen, Y., Thomsen,
899 C. and Hampson, D. R. (2013). Delayed myelination in a mouse model of fragile X
900 syndrome. *Hum. Mol. Genet.* 22, 3920–3930.

901 Pan, L., Zhang, Y. Q., Woodruff, E. and Broadie, K. (2004). The *Drosophila* fragile X gene
902 negatively regulates neuronal elaboration and synaptic differentiation. *Curr. Biol.* 14,
903 1863–1870.

904 Parvin, S., Takeda, R., Sugiura, Y., Neyazaki, M., Nogi, T. and Sasaki, Y. (2019). Fragile X
905 mental retardation protein regulates accumulation of the active zone protein Munc18-1 in
906 presynapses via local translation in axons during synaptogenesis. *Neuroscience
907 Research* 146, 36–47.

908 Patel, A. B., Hays, S. A., Bureau, I., Huber, K. M. and Gibson, J. R. (2013). A target cell-specific
909 role for presynaptic Fmr1 in regulating glutamate release onto neocortical fast-spiking
910 inhibitory neurons. *J. Neurosci.* 33, 2593–2604.

911 Pennacchio, L. A., Ahituv, N., Moses, A. M., Prabhakar, S., Nobrega, M. A., Shoukry, M.,
912 Minovitsky, S., Dubchak, I., Holt, A., Lewis, K. D., et al. (2006). In vivo enhancer analysis
913 of human conserved non-coding sequences. *Nature* 444, 499–502.

914 Peretz, Y., Eren, N., Kohl, A., Hen, G., Yaniv, K., Weisinger, K., Cinnamon, Y. and Sela-
915 Donenfeld, D. (2016). A new role of hindbrain boundaries as pools of neural
916 stem/progenitor cells regulated by Sox2. *BMC Biol* 14, 57.

917 Peretz, Y., Kohl, A., Slutsky, N., Komlos, M., Varshavsky, S. and Sela-Donenfeld, D. (2018).
918 Neural stem cells deriving from chick embryonic hindbrain recapitulate hindbrain
919 development in culture. *Sci Rep* 8, 13920.

920 Price, D. K., Zhang, F., Ashley, C. T. and Warren, S. T. (1996). The chicken FMR1 gene is
921 highly conserved with a CCT 5'-untranslated repeat and encodes an RNA-binding
922 protein. *Genomics* 31, 3–12.

923 Rais, M., Binder, D. K., Razak, K. A. and Ethell, I. M. (2018). Sensory Processing Phenotypes in
924 Fragile X Syndrome. *ASN Neuro* 10, 1759091418801092.

925 Reeber, S. L., Sakai, N., Nakada, Y., Dumas, J., Dobrenis, K., Johnson, J. E. and Kaprielian, Z.
926 (2008). Manipulating Robo expression in vivo perturbs commissural axon pathfinding in
927 the chick spinal cord. *J. Neurosci.* 28, 8698–8708.

928 Rigby, M. J., Gomez, T. M. and Puglielli, L. (2020). Glial Cell-Axonal Growth Cone Interactions
929 in Neurodevelopment and Regeneration. *Front Neurosci* 14, 203.

930 Rotschafer, S. E., Marshak, S. and Cramer, K. S. (2015). Deletion of Fmr1 Alters Function and
931 Synaptic Inputs in the Auditory Brainstem. *PLoS ONE* 10, e0117266.

932 Rotschafer, S. E., Allen-Sharp, M. R. and Cramer, K. S. (2016). Axonal Cleaved Caspase-3
933 Regulates Axon Targeting and Morphogenesis in the Developing Auditory Brainstem.
934 *Front. Neural Circuits* 10,.

935 Rubel, E. W. and Fritsch, B. (2002). Auditory system development: primary auditory neurons
936 and their targets. *Annu. Rev. Neurosci.* 25, 51–101.

937 Rubel, E. W., Smith, D. J. and Miller, L. C. (1976). Organization and development of brain stem
938 auditory nuclei of the chicken: ontogeny of n. magnocellularis and n. laminaris. *J. Comp.*
939 *Neurol.* 166, 469–489.

940 Ruby, K., Falvey, K. and Kulesza, R. J. (2015). Abnormal neuronal morphology and
941 neurochemistry in the auditory brainstem of Fmr1 knockout rats. *Neuroscience* 303,
942 285–298.

943 Sakuma, T., Nishikawa, A., Kume, S., Chayama, K. and Yamamoto, T. (2014). Multiplex
944 genome engineering in human cells using all-in-one CRISPR/Cas9 vector system. *Sci*
945 *Rep* 4,.

946 Scharkowski, F., Frotscher, M., Lutz, D., Korte, M. and Michaelson-Preusse, K. (2018). Altered
947 Connectivity and Synapse Maturation of the Hippocampal Mossy Fiber Pathway in a
948 Mouse Model of the Fragile X Syndrome. *Cereb. Cortex* 28, 852–867.

949 Schecterson, L. C., Sanchez, J. T., Rubel, E. W. and Bothwell, M. (2012). TrkB downregulation
950 is required for dendrite retraction in developing neurons of chicken nucleus
951 magnocellularis. *J. Neurosci.* 32, 14000–14009.

952 Sears, J. C. and Broadie, K. (2018). Fragile X Mental Retardation Protein Regulates Activity-
953 Dependent Membrane Trafficking and Trans-Synaptic Signaling Mediating Synaptic
954 Remodeling. *Front. Mol. Neurosci.* 10, 440.

955 Seidl, A. H., Rubel, E. W. and Barría, A. (2014). Differential Conduction Velocity Regulation in
956 Ipsilateral and Contralateral Collaterals Innervating Brainstem Coincidence Detector
957 Neurons. *J. Neurosci.* 34, 4914–4919.

958 Serafini, T., Colamarino, S. A., Leonardo, E. D., Wang, H., Beddington, R., Skarnes, W. C. and
959 Tessier-Lavigne, M. (1996). Netrin-1 Is Required for Commissural Axon Guidance in the
960 Developing Vertebrate Nervous System. *Cell* 87, 1001–1014.

961 Shamay-Ramot, A., Khremesh, K., Porath, H. T., Barak, M., Pinto, Y., Wachtel, C., Zilberberg,
962 A., Lerer-Goldshtein, T., Efroni, S., Levanon, E. Y., et al. (2015). Fmrp Interacts with
963 Adar and Regulates RNA Editing, Synaptic Density and Locomotor Activity in Zebrafish.
964 *PLOS Genetics* 11, e1005702.

965 Shepard, K. A., Korsak, L. I. T., DeBartolo, D. and Akins, M. R. (2020). Axonal localization of the
966 fragile X family of RNA binding proteins is conserved across mammals. *J. Comp. Neurol.*
967 528, 502–519.

968 Shim, S.-O., Cafferty, W. B. J., Schmidt, E. C., Kim, B. G., Fujisawa, H. and Strittmatter, S. M.
969 (2012). PlexinA2 limits recovery from corticospinal axotomy by mediating
970 oligodendrocyte-derived Sema6A growth inhibition. *Mol. Cell. Neurosci.* 50, 193–200.

971 Šmít, D., Fouquet, C., Pincet, F., Zapotocky, M. and Trembleau, A. (2017). Axon tension
972 regulates fasciculation/defasciculation through the control of axon shaft zippering. *eLife*
973 6, e19907.

974 Stoeckli, E. T. (2018). Understanding axon guidance: are we nearly there yet? *Development*
975 145, dev151415.

976 [Strumbos, J. G., Brown, M. R., Kronengold, J., Polley, D. B. and Kaczmarek, L. K. \(2010\).
977 Fragile X Mental Retardation Protein Is Required for Rapid Experience-Dependent
978 Regulation of the Potassium Channel Kv3.1b. *Journal of Neuroscience* 30, 10263–
979 10271.](#)

980 Tessier, C. R. and Broadie, K. (2008). Drosophila fragile X mental retardation protein
981 developmentally regulates activity-dependent axon pruning. *Development* 135, 1547–
982 1557.

983 Varadarajan, S. G., Kong, J. H., Phan, K. D., Kao, T.-J., Panaitof, S. C., Cardin, J., Eltzschig,
984 H., Kania, A., Novitsch, B. G. and Butler, S. J. (2017). Netrin1 Produced by Neural

985 Progenitors, Not Floor Plate Cells, Is Required for Axon Guidance in the Spinal Cord.
986 *Neuron* 94, 790-799.e3.

987 Vonderschen, K. and Wagner, H. (2014). Detecting interaural time differences and remodeling
988 their representation. *Trends in Neurosciences* 37, 289–300.

989 Wang, Z. and Storm, D. R. (2006). Extraction of DNA from mouse tails. *BioTechniques* 41, 410,
990 412.

991 Wang, Y. and Rubel, E. W. (2012). In Vivo Reversible Regulation of Dendritic Patterning by
992 Afferent Input in Bipolar Auditory Neurons. *Journal of Neuroscience* 32, 11495–11504.

993 Wang, W., Bradley, A. and Huang, Y. (2009). A piggyBac transposon-based genome-wide
994 library of insertionally mutated Blm-deficient murine ES cells. *Genome Research* 19,
995 667–673.

996 Wang, J., Miller, E. D., Simmons, G. S., Miller, T. A., Tabashnik, B. E. and Park, Y. (2010).
997 piggyBac-like elements in the pink bollworm, *Pectinophora gossypiella*. *Insect Mol. Biol.*
998 19, 177–184.

999 Wang, Y., Sakano, H., Beebe, K., Brown, M. R., de Laat, R., Bothwell, M., Kulesza, R. J. and
1000 Rubel, E. W. (2014). Intense and specialized dendritic localization of the fragile X mental
1001 retardation protein in binaural brainstem neurons: a comparative study in the alligator,
1002 chicken, gerbil, and human. *J. Comp. Neurol.* 522, 2107–2128.

1003 Wang, T., de Kok, L., Willemsen, R., Elgersma, Y. and Borst, J. G. G. (2015a). In vivo synaptic
1004 transmission and morphology in mouse models of Tuberous sclerosis, Fragile X
1005 syndrome, Neurofibromatosis type 1, and Costello syndrome. *Front. Cell. Neurosci.* 9,.

1006 Wang, B., Pan, L., Wei, M., Wang, Q., Liu, W.-W., Wang, N., Jiang, X.-Y., Zhang, X. and Bao, L.
1007 (2015b). FMRP-Mediated Axonal Delivery of miR-181d Regulates Axon Elongation by
1008 Locally Targeting Map1b and Calm1. *Cell Reports* 13, 2794–2807.

1009 Wang, X., Zorio, D. A. R., Schecterson, L., Lu, Y. and Wang, Y. (2018). Postsynaptic FMRP
1010 Regulates Synaptogenesis In Vivo in the Developing Cochlear Nucleus. *J. Neurosci.* 38,
1011 6445–6460.

1012 Wang, X., Hong, H., Brown, D. H., Sanchez, J. T. and Wang, Y. (2017). Distinct Neural
1013 Properties in the Low-Frequency Region of the Chicken Cochlear Nucleus
1014 Magnocellularis. *eNeuro* 4,.

1015 Wang, X., Zorio, D. A. R., Schecterson, L., Lu, Y. and Wang, Y. (2018). Postsynaptic FMRP
1016 Regulates Synaptogenesis In Vivo in the Developing Cochlear Nucleus. *J. Neurosci.* 38,
1017 6445–6460.

1018 Weisinger, K., Kohl, A., Kayam, G., Monsonego-ornan, E. and Sela-donenfeld, D. (2012).
1019 Expression of hindbrain boundary markers is regulated by FGF3. *Biology Open* 1, 67–
1020 74.

1021 Wurster, S., Kumaresan, P. R., Albert, N. D., Hauser, P. J., Lewis, R. E. and Kontoyiannis, D. P.
1022 (2019). Live Monitoring and Analysis of Fungal Growth, Viability, and Mycelial
1023 Morphology Using the IncuCyte NeuroTrack Processing Module. *mBio* 10, e00673-19,
1024 /mbio/10/3/mBio.00673-19.atom.

1025 Xu, B., Zhang, Y., Zhan, S., Wang, X., Zhang, H., Meng, X. and Ge, W. (2018). Proteomic
1026 Profiling of Brain and Testis Reveals the Diverse Changes in Ribosomal Proteins in *fmr1*
1027 Knockout Mice. *Neuroscience* 371, 469–483.

1028 Xu, J., Berret, E. and Kim, J. H. (2017). Activity-dependent formation and location of voltage-
1029 gated sodium channel clusters at a CNS nerve terminal during postnatal development. *J.*
1030 *Neurophysiol.* 117, 582–593.

1031 Young, S. R. and Rubel, E. W. (1986). Embryogenesis of arborization pattern and topography of
1032 individual axons in N. Laminaris of the chicken brain stem. *J. Comp. Neurol.* 254, 425–
1033 459.

1034 Yu, X., Wang, X., Sakano, H., Zorio, D. A. R. and Wang, Y. (2020). Dynamics of the Fragile X
1035 Mental Retardation Protein Correlates with Cellular and Synaptic Properties in Primary
1036 Auditory Neurons following Afferent Deprivation. *Journal of Comparative Neurology*. doi:
1037 [10.1002/cne.24959](https://doi.org/10.1002/cne.24959). Online ahead of print.

1038 Yung, A. R., Druckenbrod, N. R., Cloutier, J.-F., Wu, Z., Tessier-Lavigne, M. and Goodrich, L. V.
1039 (2018). Netrin-1 Confines Rhombic Lip-Derived Neurons to the CNS. *Cell Reports* 22,
1040 1666–1680.

1041 Zimmer, S. E., Doll, S. G., Garcia, A. D. R. and Akins, M. R. (2017). Splice form-dependent
1042 regulation of axonal arbor complexity by FMRP. *Dev Neurobiol* 77, 738–752.

1043 Zorio, D. A. R., Jackson, C. M., Liu, Y., Rubel, E. W. and Wang, Y. (2017). Cellular distribution
1044 of the fragile X mental retardation protein in the mouse brain. *J. Comp. Neurol.* 525,
1045 818–849.

1046
1047 **Figure legends**

1048 **Figure 1. High-specificity genetic labeling of NM precursors and neurons. A.** Schematic
1049 drawing of the NM-NL circuit. **B.** Plasmid design for Atoh1-mGFP. Electroporation is performed
1050 following plasmid injection into rhombomeres 5-6 (r5-6; dark blue). **C.** E15 brainstem sections
1051 showing a restricted localization of mGFP⁺ cell bodies in NM on the transfection (ipsi) side.

1052 Yellow stars indicate bilateral NM axons to NL. **E. Ratio of transfected neurons in NM.** The
1053 mean value is indicated for this and all plots in subsequent figures. Abbreviations: ANF, auditory
1054 nerve fiber; ipsi, ipsilateral; contra, contralateral. Scale bar: 200 μm in C.

1055
1056 **Figure 2. Axon development of NM precursors and neurons.** Images were taken from
1057 embryos electroporated with Atoh1-mGFP at E2-2.5. **A.** Flat-mount view at E4.5 showing two
1058 contralateral projection bundles (LF and DF) of Atoh1/dA1 cells. **B.** Top view at E5 showing that
1059 axons of Atoh1/dA1 cells at r5-6 join the DF bundle. Dashed lines indicate the midline. **C.**
1060 Transverse section at E4 at the level of r5-6. mGFP⁺ axons have crossed the midline and
1061 arrived in their contralateral target area (yellow arrow). **D.** An illustration describing the
1062 measurements used to quantify axonal growth patterns of NM precursors. Axon bundle width
1063 was calculated as the ratio between B (GFP⁺ fascicule width) divided by A (mantle-ventricular
1064 width). Axonal midline crossing rate was calculated as D (area of GFP⁺ contralateral axons)
1065 divided by C (area of GFP⁺ ipsilateral axons). A° was the angle between the most medial GFP⁺
1066 projecting axon and the mantle plate. **E-F.** Box plot analysis of the ratio of axonal midline
1067 crossing (E) and bundle width (F) of Atoh1:cre tagged axons at E4.5. Each data point
1068 represents one embryo (n=7). **G.** Plasmid design for SV2-GFP with Atoh1-enhancer and
1069 PiggyBac (PB) transposase. **H-I'.** SV2-GFP (green) distribution in transverse sections
1070 counterstained with NeuroTrace (magenta) on the ipsilateral (H-H') and contralateral (I-I') sides.
1071 H' and I' are enlarged views of the boxes in H and I, respectively. NM is outlined by dashed
1072 circles. The cell body layer (c) as well as the dorsal (d) and ventral (v) dendrite domains of the
1073 NL are indicated. Abbreviations: LF, lateral funiculus; DF, dorsal funiculus. Scale bars: 1 mm in
1074 A (applies to A-B) and C; 100 μm in H and I; 20 μm in H' and I'.

1075
1076 **Figure 3: Morphological maturation of presynaptic terminals of NM neurons.** Images were
1077 taken from embryos electroporated with Atoh1-mGFP at E2. **A-B.** NM axon terminals in the
1078 dorsal neuropil of the ipsilateral NL (A) and in the ventral neuropil of the contralateral NL (B) at
1079 E12 and E15. NM axons show a growth cone structure with filopodia (white arrows) at E12 and
1080 bouton-like terminals (yellow arrows) at E15. **C-D.** Frequency distribution (B) and population
1081 analysis (C) of the number of filopodia per terminal at E11-13 (n=51 terminals) and E15 (n=42
1082 terminals). Additional images and data analyses are shown in Figs. S3,S4. Scale bars: 2 μm .

1083
1084 **Figure 4. Endogenous FMRP is localized in distal axons of NM precursors.** **A.** FMRP
1085 immunostaining taken from an E4 embryo. **B-B''.** FMRP immunostaining (B') taken from an E5

1086 embryo transfected with Atoh1-mGFP (B). B'' is the merged image. Note the FMRP
1087 immunostaining in the region where transfected cell bodies are located (green arrows). The
1088 terminal region on the contralateral side (yellow arrows) is low in FMRP immunoreactivity. **C-C''**.
1089 High-magnification images of the box in B'' from the transfection (ipsi) side. Transfected cells
1090 (green) contain FMRP immunoreactivity (red) in the cytoplasm (c in insets) and a weaker
1091 staining in the nuclear (n in insets). **D-D''**. High-magnification images of the box in B'' from the
1092 contralateral side (contra). **A subset of FMRP puncta are localized in mGFP⁺ axon processes**
1093 **(insets). FMRP puncta that are localized beyond mGFP⁺ axon processes are presumably in**
1094 **untransfected axons because this region contains no cell bodies as indicated with the lack of**
1095 **DAPI-labeled nuclei. E. Colocalization analysis of a representative FMRP punctum with Atoh1-**
1096 **mGFP⁺ labeled axon, confirming the axonal location of FMRP.** Scale bars: 100 μ m in A; 200 μ m
1097 in B'' (applies to B-B''); 5 μ m in C and D (applies to C-D''); 2 μ m for insets; 1 μ m in E.

1098
1099 **Figure 5. Axon localization of FMRP in NM neurons. A.** Plasmid designs for constitutive
1100 expression of chicken and human FMRP (chFMRP and hFMRP). **B.** Schematic drawing of the
1101 co-transfection protocol for chFMRP-mCherry and Atoh1-mGFP. **C.** Transverse sections at E15
1102 showing transfected cell bodies in NM (left column) and their contralateral projection in NL (right
1103 column), following the co-transfection shown in B. White arrow indicates a co-transfected NM
1104 neuron. On the contralateral side, chFMRP-mCherry puncta are detected within the ventral
1105 neuropil domain of NL as well as the fiber region containing incoming NM axons. **D.** High
1106 magnification images of the ventral neuropil of the contralateral NL at E11 and E15. A subset of
1107 FMRP-mCherry puncta are located in Atoh1-mGFP⁺ NM axons (arrows). **E.** Images of the
1108 contralateral NL at E15 following transfection with hFMRP-EGFP and MAP2 counterstaining
1109 (red), a somatodendritic marker. hFMRP puncta are distributed in the ventral fiber region and
1110 the ventral NL neuropil. Abbreviation: MAP2, microtubule-associated protein 2. Scale bars: 100
1111 μ m in the left column of C; 20 μ m in the right column of C; 5 μ m in D; 50 μ m in E; 7.5 μ m in
1112 inset.

1113
1114 **Figure 6. FMRP knockout with Crispr/Cas9 strategy. A.** Crispr design of FMRP sequence in
1115 exon 8. **B.** Gel electrophoresis of PCR products from hindbrains electroporated with gRNA_{control}
1116 and gRNA₃₊₄ plasmids. Red arrow points to a ~260 bp fragment obtained by Cas9 deletion. **C-D.**
1117 Sagittal-section views of E6.5 brainstems expressing gRNA_{control} (C) or gRNA₃₊₄ (D) plasmids
1118 (green) and stained for FMRP antibody (red). High-magnification views of the boxed areas in C-
1119 D and C'-D' appear in the right panel of each image. Arrows and arrowheads point to FMRP⁺

1120 and FMRP⁺ cells, respectively. **E.** Box plot quantification of FMRP-immunoreactive cells out of
1121 total GFP⁺ cells. Each data point represents one embryo (n=7 embryos for each group). **F-G.**
1122 Cross-section views of E4.5 hindbrains obtained from embryos that were electroporated with
1123 gRNA_{control} or gRNA₃₊₄ (F-G, green) and stained with Lhx2/9 antibody (red). Higher-magnification
1124 views of the boxed areas in F and G are represented in the right of each panel in different
1125 channels. Arrows indicate the same cells in all channels. **H.** Box plot quantification of Lhx2/9
1126 immunoreactive cells out of total GFP⁺ cells. Each data point represents one section (n=3
1127 embryos for each group). Scale bars: 100 μm in C (applies to C-D) and G (applies to F-G); 50
1128 μm in C' (applies to C'-D'); 20 μm in C'' (applies to C''-D''); 50 μm in insets in F, G.

1129

1130 **Figure 7. Crispr-mediated FMRP knockout induces disoriented axonal growth. A-B.** E4.5
1131 flat-mounted hindbrains from embryos electroporated at E2.5 with gRNA_{control} (A) or gRNA₃₊₄ (B).
1132 Higher-magnification views of the boxed areas in A, B are represented at A', B'. Arrows point to
1133 organized axons in A. Dashed arrows in B' indicate disoriented axons. **C-G'.** Transverse
1134 sections of r5-6 level at E4.5 (C-E') and E6.5 (F-G') from embryos electroporated with
1135 gRNA_{control} (C-C', F-F') or gRNA₃₊₄ (D-E', G-G') plasmids. Higher-magnification views of the
1136 boxed areas in the left panels (C-G) are represented in the right panels (C'-G'). Arrows in the
1137 left panels indicate axons that crossed the midline. Arrows and arrowheads in the right panels
1138 point to organized and disorganized axons, respectively. **H-I.** Box plot analysis of the width of
1139 the GFP⁺ axonal bundle at E4.5 (H) and E6.5 (I). **J-K.** Box plot analysis of the axonal midline
1140 crossing rate at E4.5 (J) and E6.5 (K). Each data point represents one embryo. Abbreviation:
1141 FP, floor plate. Scale bars = 100 μm in A (applies to A, B); 50 μm in A' (applies to A', B'); 100
1142 μm in C (applies to C, D, E, F, G); 50 μm in C' (applies to C', D', E', F', G').

1143

1144 **Figure 8. shRNA-mediated FMRP knockdown induces axonal disorganization. A-B.** E4.5
1145 flat-mounted hindbrains from embryos that were electroporated at E2.5 with scrambled-shRNA-
1146 EGFP (sc-shRNA; A) or *Fmr1*-shRNA-EGFP (B). Higher-magnification views of the boxed areas
1147 in A, B are represented at A', B'. Plasmid design for *Fmr1*-shRNA is illustrated on the top.
1148 Arrows and dashed arrows represent organized and disoriented axons, respectively. **C-G'.**
1149 Transverse sections of r5-r6 level at E4.5 (C-E') and E6.5 (F-G') from embryos electroporated
1150 with sc-shRNA (C-C', F-F') or *Fmr1*-shRNA (D-E', G-G') plasmids. Higher-magnification views of
1151 the boxed areas in the left panels (C-G) are represented in the right panels (C'-G'). Arrows in
1152 left panels indicate axons that crossed the midline. Arrows and arrowheads in the right panels
1153 point to organized and disorganized axons, respectively. **H-I.** Box plot analysis of the width of

1154 the GFP⁺ axonal bundle at E4.5 (H) and E6.5 (I). **J-K.** Box plot analysis of the axonal midline
1155 crossing rate at E4.5 (J) and E6.5 (K). Each data point presents one embryo. Abbreviation: FP,
1156 floor plate. Scale bars: 100 μm in A (applies to A, B); 50 μm in A' (applies to A', B'); 100 μm in C
1157 (applies to C, D, E, F, G); 50 μm in C' (applies to C', D', E', F', G').

1158
1159 **Figure 9. Crispr-mediated FMRP knockout induces neurite overgrowth and**
1160 **overbranching in hindbrain culture. A-H'.** Time-lapse analysis of cell cultures obtained from
1161 E3.5 hindbrains that were electroporated at E2.5 with gRNA_{control} (A, C, E, G) and gRNA₃₊₄ (B,
1162 D, F, H) plasmids. Cells were documented every 6 hours for 5 days. Representative phase and
1163 green fluorescence images in different time points are shown. GFP⁺ neurites are evident in all
1164 images. **I-L.** Higher-magnification views of the boxed areas in above panels (E-H) are
1165 represented in the bottom panels, respectively. Arrows in panels (K, L) show overbranching
1166 along the neurite up to its terminal. **M-N.** Quantification of neurite branch point (M) and neurite
1167 length (N) along 5 days using NeuroTrack analysis. Each data point represents 6 different wells
1168 of a 48-well plate. Scale bars: 200 μm in H' (applies to A-H'); 50 μm in L (applies to I-L).

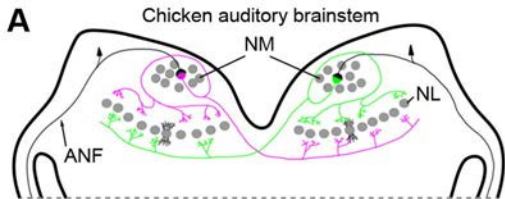
1169
1170 **Figure 10. FMRP knockdown leads to axon projection errors in NL. A.** Transfection protocol
1171 for late-onset shRNA expression. Blue arrows point out the days for Dox treatment. **B-C.**
1172 Schematic drawings of normal (B) and aberrant (C) axon targeting of NM neurons in the
1173 contralateral NL. **D-E.** Photomicrographs of NM axons in the contralateral NL at E15 following
1174 scrambled-shRNA (D) and *Fmr1*-shRNA (E) expression. Arrows point to abnormally projected
1175 NM axons through the cell body layer into the dorsal neuropil. **F.** NM axons in the contralateral
1176 NL at E19 following *Fmr1*-shRNA expression. The axons are predominantly distributed in the
1177 ventral neuropil, similar to the control. Dashed lines indicate the cell body layer. **G.**
1178 Quantification of the dorsal/ventral ratio of axon area. This ratio is significantly increased in
1179 *Fmr1*-shRNA transfected embryos at E15 (red squares) but not E19 (blue triangles), as
1180 compared to control embryos (black circles). Scale bars: 50 μm in D, E, F.

1181
1182 **Figure 11. Aberrantly projected NM axons form synapses on NL dendrites.** NM precursors
1183 were unilaterally transfected with *Fmr1*-shRNA-EGFP. Images were taken from the side
1184 contralateral to the transfection. **A-A'.** Images of a dye-filled NL neuron (red) whose dorsal and
1185 ventral dendrites are in close contact with EGFP⁺ NM axons (white arrows). **B-B'.** Double
1186 labeling of Syt2 immunoreactivity with EGFP⁺ NM axons. Stars indicate NL cell bodies in B'.
1187 Higher-magnification views of the boxed area in I' are represented in the right panels. EGFP⁺

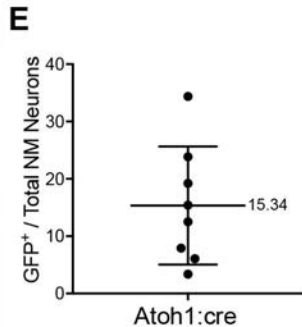
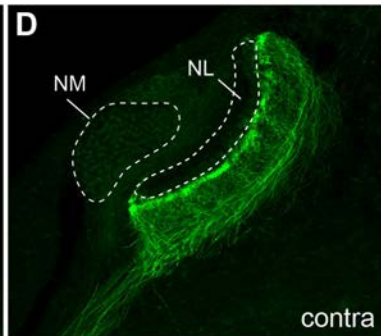
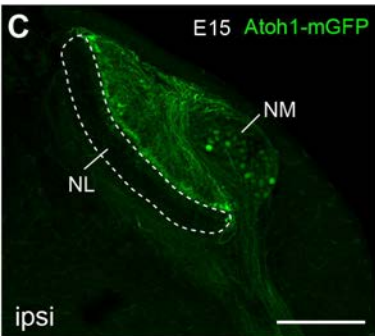
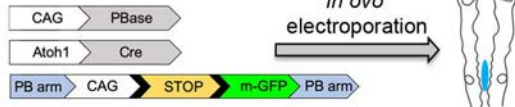
1188 axonal terminals (white arrows) are immunoreactive to Syt2. Scale bars: 10 μm in A, 2 μm in
1189 inset of A', 20 μm in B, and 2 μm in the right most column. Abbreviation: Syt 2, synaptotagmin
1190 2.

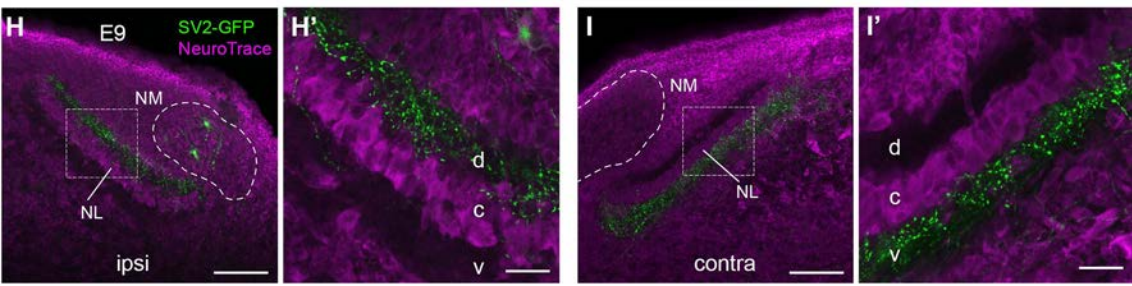
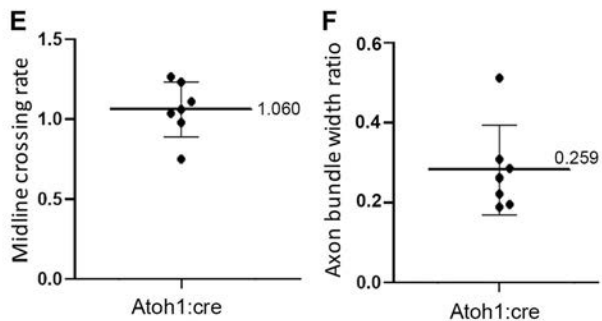
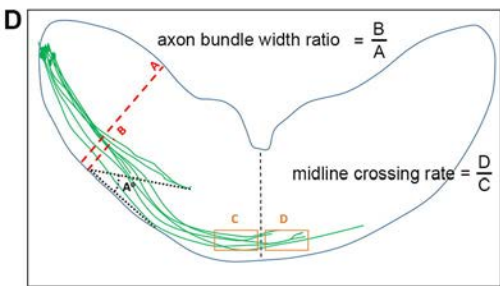
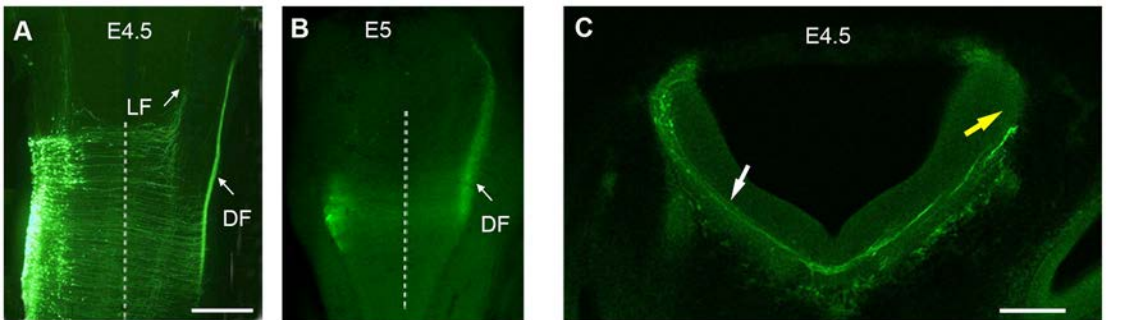
1191

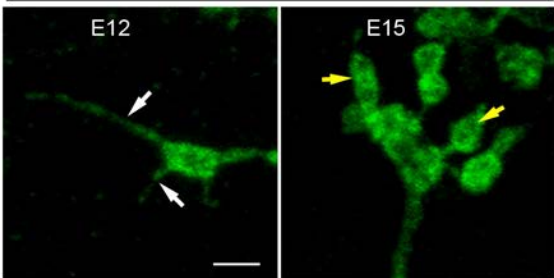
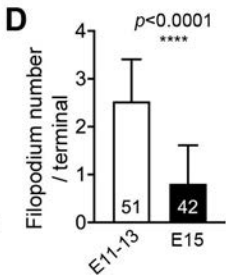
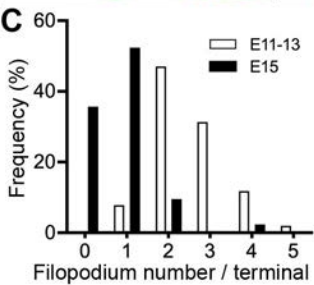
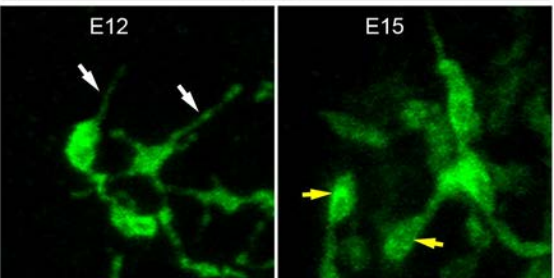
1192 **Figure 12. FMRP knockdown does not affect the morphological maturation of NM axonal**
1193 **terminals. A-B.** Frequency distribution (A) and population analysis (B) of the number of
1194 filopodia per terminal following transfection with *Atoh1:cre-mGFP* (black bars; n=21 terminals)
1195 and *Fmr1-shRNA* (green bars; n=14 terminals). All terminals were measured from the ventral
1196 neuropil of the contralateral NL.

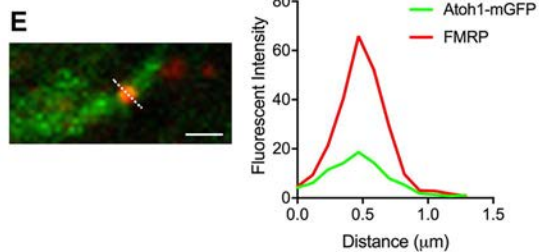
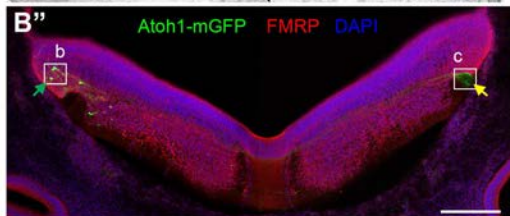
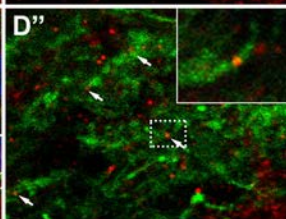
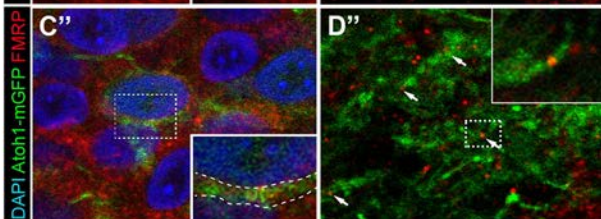
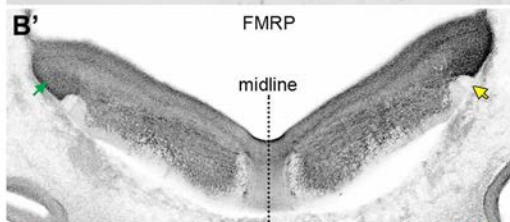
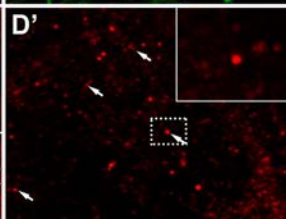
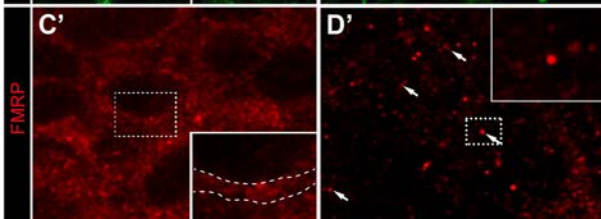
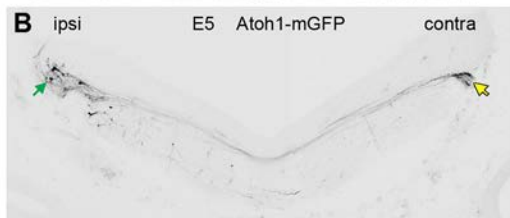
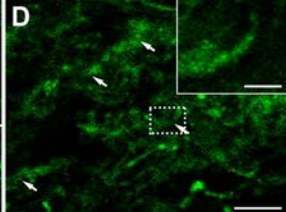
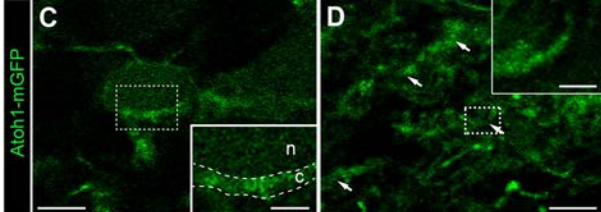
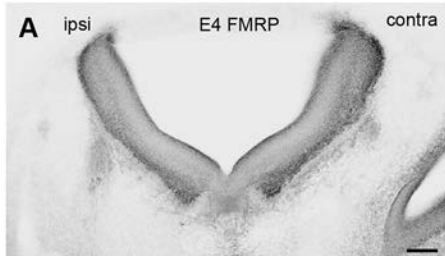


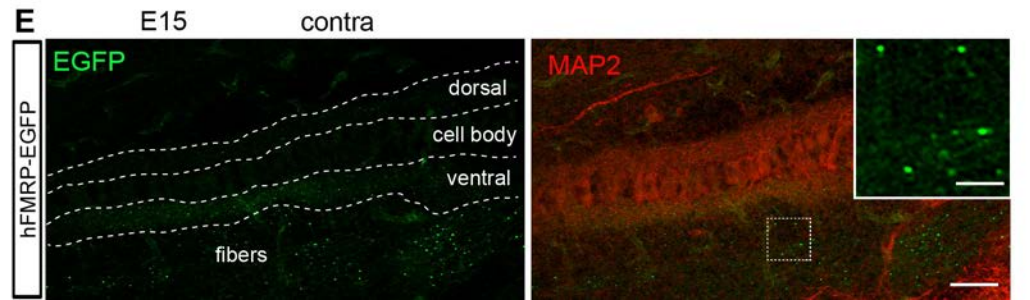
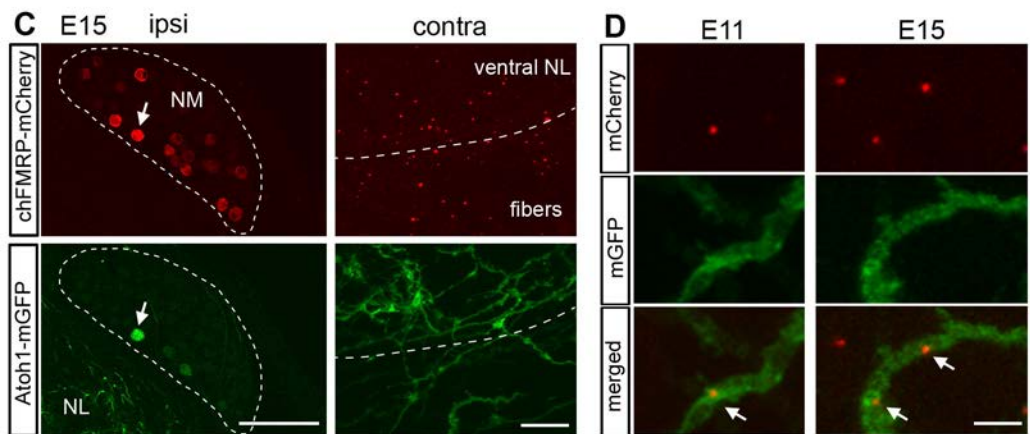
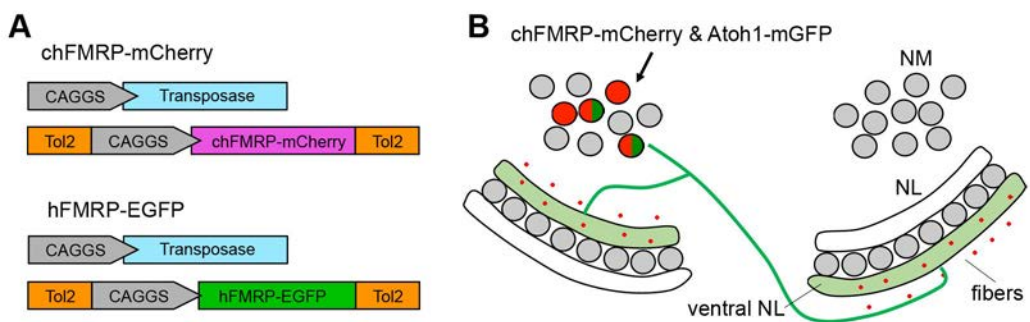
B Atoh1 promotor-driven constructs

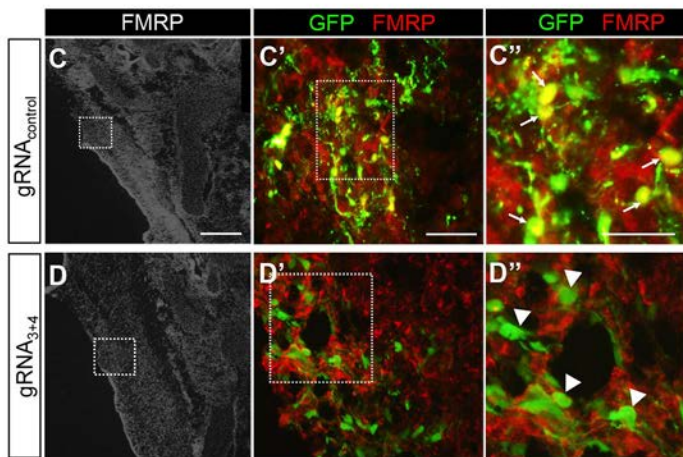
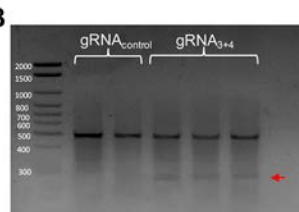
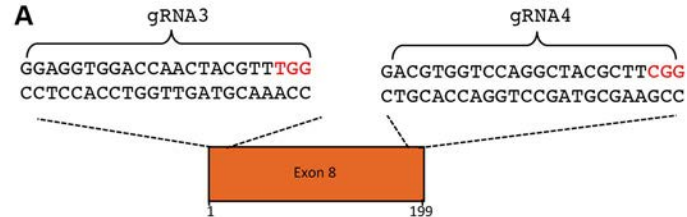




A ipsi**B** contra







E Ratio of FMRP⁺ cells

